iScience

CellPress
OPEN ACCESS

Article

RNA helicase DDX3 regulates RAD51 localization and DNA damage repair in Ewing sarcoma

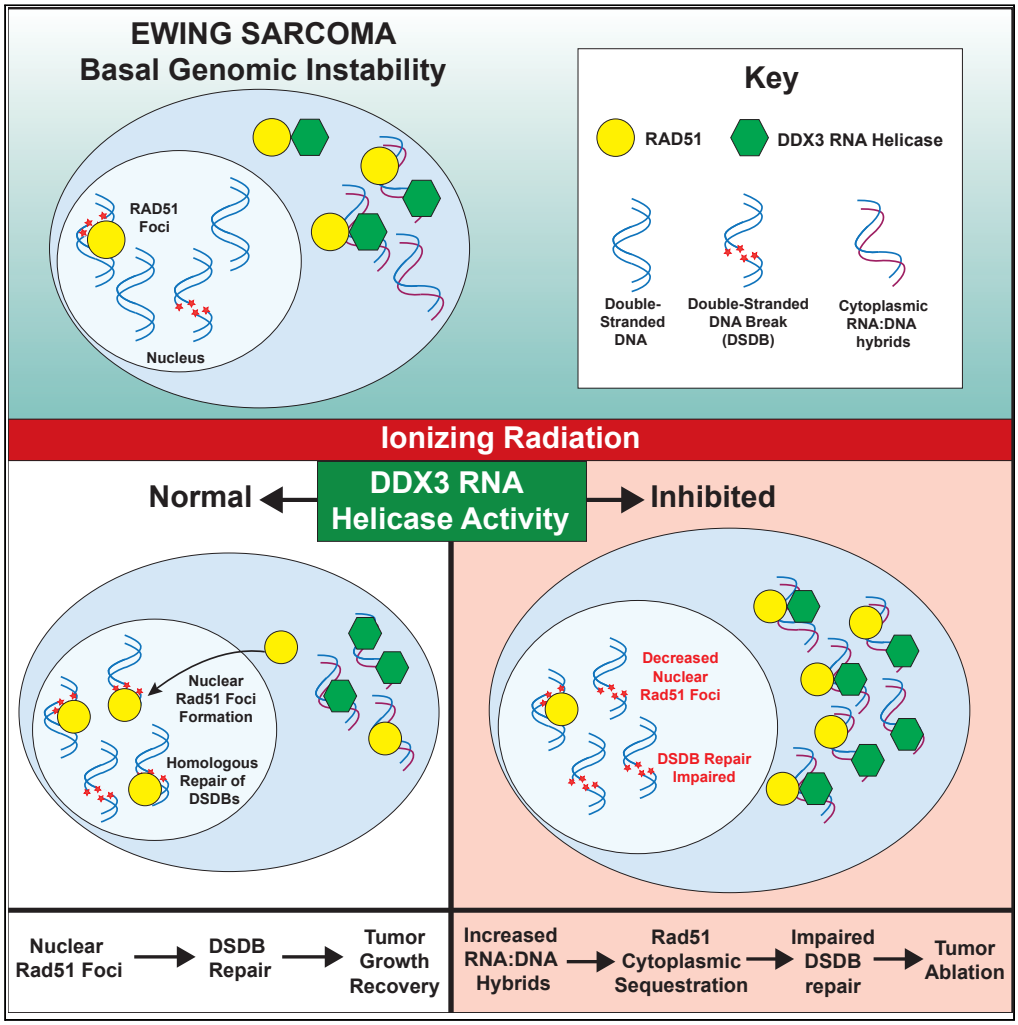

Matthew E. Randolph, Marwa Afifi, Aparna Gorthi, ..., Venu Raman, Alexander J.R. Bishop, David M. Loeb

david.loeb@einsteinmed.edu

Highlights

Impaired DDX3 RNA helicase activity induces radiosensitization of Ewing sarcoma *in vivo*

DDX3 inhibition attenuates homologous repair and augments radiation-induced cell death

DDX3 alters RAD51 localization by modulating cytoplasmic RNA:DNA hybrid abundance

RK-33 inhibits DDX3 and sequesters RAD51 in the cytoplasm, preventing DNA damage repair

Randolph et al., iScience 27, 108925
February 16, 2024 © 2024
https://doi.org/10.1016/j.isci.2024.108925

iScience

CellPress
OPEN ACCESS

Article

RNA helicase DDX3 regulates RAD51 localization and DNA damage repair in Ewing sarcoma

Matthew E. Randolph,[1,2] Marwa Afifi,[3] Aparna Gorthi,[4] Rachel Weil,[1] Breelyn A. Wilky,[5] Joshua Weinreb,[1] Paul Ciero,[1,2] Natalie ter Hoeve,[7] Paul J. van Diest,[7] Venu Raman,[5,6,8] Alexander J.R. Bishop,[4] and David M. Loeb[1,2,5,9,*]

SUMMARY

We previously demonstrated that RNA helicase DDX3X (DDX3) can be a therapeutic target in Ewing sarcoma (EWS), but its role in EWS biology remains unclear. The present work demonstrates that DDX3 plays a unique role in DNA damage repair (DDR). We show that DDX3 interacts with several proteins involved in homologous recombination, including RAD51, RECQL1, RPA32, and XRCC2. In particular, DDX3 colocalizes with RAD51 and RNA:DNA hybrid structures in the cytoplasm of EWS cells. Inhibition of DDX3 RNA helicase activity increases cytoplasmic RNA:DNA hybrids, sequestering RAD51 in the cytoplasm, which impairs nuclear translocation of RAD51 to sites of double-stranded DNA breaks, thus increasing sensitivity of EWS to radiation treatment, both *in vitro* and *in vivo*. This discovery lays the foundation for exploring new therapeutic approaches directed at manipulating DDR protein localization in solid tumors.

INTRODUCTION

Ewing sarcoma (EWS) is the second most common high-grade bone sarcoma in children and adolescents. Overall survival of EWS patients is less than 30% for patients with metastatic or recurrent disease despite aggressive chemotherapy, radiation, and/or surgery.[1,2] EWS is characterized by a chromosomal translocation of the EWS RNA binding protein 1 (*EWSR1*) with an erythroblast-transformation-specific (*ETS*) family gene or ETS-related gene such as Friend leukemia integration 1 transcription factor (*FLI-1*) or transcriptional regulator (*ERG*), in 85% and 10% of all EWS cases, respectively.[1] The resultant fusion protein acts as a driver for the oncologic biology of EWS with few somatic mutations contributing to the phenotype.[3,4] To date, no systemic therapies exist that prolong overall survival of children with metastatic or recurrent EWS. New therapeutic targets, or approaches that increase the potency or effectiveness of current therapeutics, are desperately needed.

DEAD/H box RNA helicases are a superfamily of ATPase-dependent RNA helicases that have a conserved amino acid sequence (Asp-Glu-Ala-Asp/His). These RNA helicases unwind and remodel RNA:RNA duplexes, RNA:DNA hybrids, and messenger ribonucleoprotein complexes.[5,6] ATP-dependent RNA helicases, such as DDX3X (DDX3), are ubiquitous enzymes involved in multiple facets of RNA metabolism and are increasingly recognized as important contributors to cancer pathogenesis.[7,8] DDX3 has been specifically implicated in the pathogenesis of EWS.[9,10] We have previously demonstrated that multiple sarcoma cell lines, including EWS, and primary-sarcoma-patient-derived xenograft (PDX) models express high levels of DDX3.[10] We have also shown that treatment with RK-33, a small molecule inhibitor of DDX3 RNA helicase activity,[11–13] is selectively cytotoxic to EWS cell lines, compared with normal mesenchymal cells.[10] Additionally, RK-33 sensitivity in PDX models correlates with DDX3 expression,[10] suggesting that interfering with DDX3 function may be a viable treatment strategy for EWS.

To further understand the underlying mechanisms of this phenotype, proteomic analysis of EWS cell lines with either shRNA knockdown or chemical inhibition of DDX3 was performed. These studies revealed several cellular pathways that are affected by DDX3 impairment, one of which is the DNA damage repair (DDR) pathway.[10] Induction of DNA damage via ionizing radiation (IR) is a treatment modality for a subset of EWS patients with recurrent or metastatic disease[14] as well as for patients with unresectable primary tumors.[15] Therefore, we investigated whether DDX3 contributes to DDR in EWS and if impairment of DDX3 helicase activity with RK-33 in EWS could be leveraged as a radiosensitizing strategy.

[1]Department of Developmental and Molecular Biology, Albert Einstein College of Medicine, Bronx, NY, USA
[2]Department of Pediatrics, Albert Einstein College of Medicine, Bronx, NY, USA
[3]Laboratory of Cancer Biology and Genetics, Center for Cancer Research, National Cancer Institute, Bethesda, MD, USA
[4]Greehey Children's Cancer Research Institute and Department of Cell Systems & Anatomy, UT Health San Antonio, San Antonio, TX, USA
[5]Department of Oncology, Sidney Kimmel Comprehensive Cancer Center, Johns Hopkins University, Baltimore, MD, USA
[6]Department of Radiology, Johns Hopkins University, Baltimore, MD, USA
[7]Department of Pathology, University Medical Centre Utrecht, Utrecht, the Netherlands
[8]Department of Pharmacology, Johns Hopkins University, Baltimore, MD, USA
[9]Lead contact
*Correspondence: david.loeb@einsteinmed.edu
https://doi.org/10.1016/j.isci.2024.108925

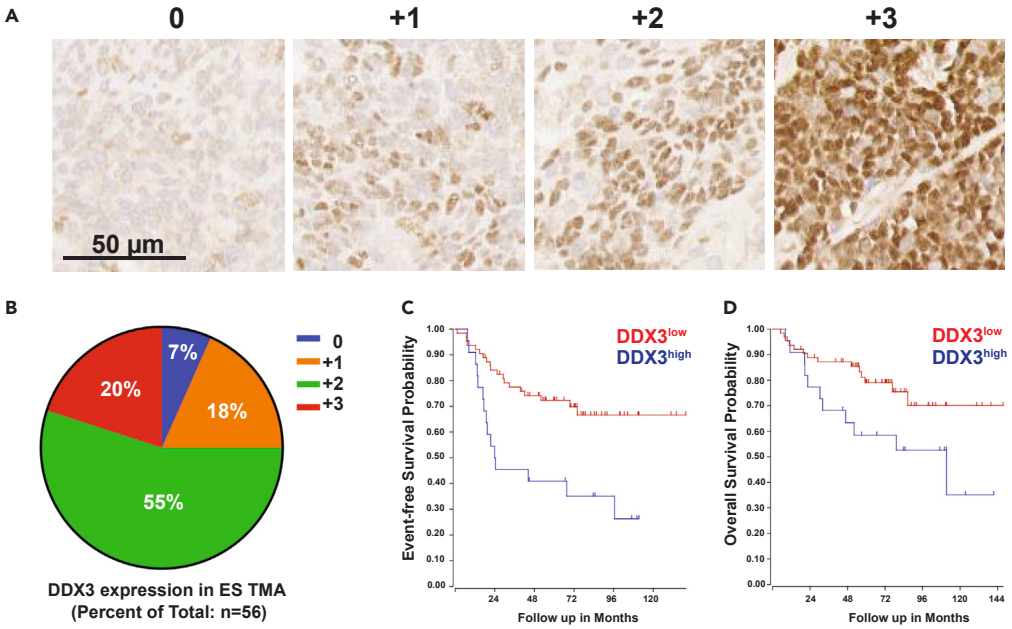

Figure 1. Elevated DDX3 expression in Ewing sarcoma is associated with poor prognosis

(A) Immunohistochemical staining of Ewing sarcoma tissue microarray (TMA). Representative images of DDX3 protein expression described subjectively on a range of staining intensity: 0 (no staining), +1 (low), +2 (moderate), or +3 (high). Mag bar: 50 μm.

(B) Pie chart showing the distribution of DDX3 expression among TMA samples (n = 56).

(C and D) Kaplan-Meier curves demonstrating event-free survival (EFS) and overall survival (OS) of EWS patients' tumors with either low (red) (n = 63) or high (blue) (n = 22) levels of DDX3X mRNA transcripts. EFS: raw p = 0.0014 by log rank (Mantel-Cox) test. OS: raw p = 0.044 by log rank (Mantel-Cox) test.

RESULTS

Expression of DDX3 is prevalent in EWS patients and is negatively associated with long-term survival

Previously, we demonstrated that multiple sarcoma cell lines and primary sarcoma PDX models express high levels of DDX3[10]; however, the frequency and significance of DDX3 expression in EWS patient samples had not been assessed. To determine whether DDX3 expression is prevalent in EWS patients, immunohistochemical analysis of DDX3 expression was performed using an EWS tissue microarray. High DDX3 expression was present in majority of EWSs examined (Figures 1A and 1B). To evaluate the prognostic impact of DDX3 expression in EWS patients, we analyzed a previously reported dataset (GEO ID: gse63157) of mRNA transcripts obtained from EWS patients[16] using the R2 Genomics Platform (https://r2.amc.nl). Elevated DDX3 mRNA levels correlated with worse event-free (p = 0.0014) and overall survival (p = 0.044) rates compared with patients whose tumors expressed low levels of DDX3 mRNA (Figures 1C and 1D). This correlation further supports the clinical value of targeting DDX3 function as a potentially beneficial therapy for EWS patients.

Double-stranded DDR is abrogated by inhibition of DDX3 helicase activity following IR

To elucidate the underlying contribution of DDX3 function to EWS biology, we previously used a proteomic approach to identify cellular pathways/processes in EWS that were uniformly altered with both genetic and chemical inhibition of DDX3.[10] One of the major cellular processes altered with DDX3 inhibition was DDR.[10] To examine the effects of DDX3 inhibition on DDR, we irradiated (2 Gy) EWS cell lines that either stably expressed shRNA against DDX3[10] or were treated with RK-33. Resultant double-stranded DNA breaks were quantified via the immunofluorescent presence of phosphorylated histone H2A variant H2A.X (γ-H2A.X) foci (Figure 2A).[17] To inhibit DDX3 function genetically, we utilized our previously established stable DDX3 knockdown MHH-ES-1 EWS cell lines that constitutively express shDDX3 with a verified knockdown (KD) of 70%–80% by western blot.[10] In the presence of decreased constitutive levels of DDX3, we observed both higher basal levels of γ-H2A.X foci in KD versus control cell lines and impairment of $DDX3^{KD}$ cells to resolve γ-H2A.X foci by 24 h post-IR, suggesting DDX3 contributes to the maintenance of genomic integrity in EWS (Figure 2B). Additionally, chemical inhibition of DDX3 RNA helicase activity with RK-33 treatment significantly inhibited the restoration of double-stranded DNA break abundance back to basal levels within 24 h of IR in three independent EWS cell lines (Figure 2C). Although the overall effect was consistent, the magnitude of the inhibition varied among the three EWS cell lines, as would be expected in a clinical setting. Importantly, clonogenic assays demonstrated that survival of EWS cells was significantly impaired following the combined treatment of RK-33 with IR (Figures 2D and 2E). Thus, pharmacologic or genetic inhibition of DDX3 attenuates DDR in EWS cells, resulting in increased cell death.

Because inhibition of DDX3 impairs the repair of double-stranded DNA breaks up to 24 h after IR, we tested whether chemical impairment of DDX3 with RK-33 could serve as a radiosensitizing approach in EWS PDX models. Two EWS PDX models, EWS4 and JHH-ESX-3 that

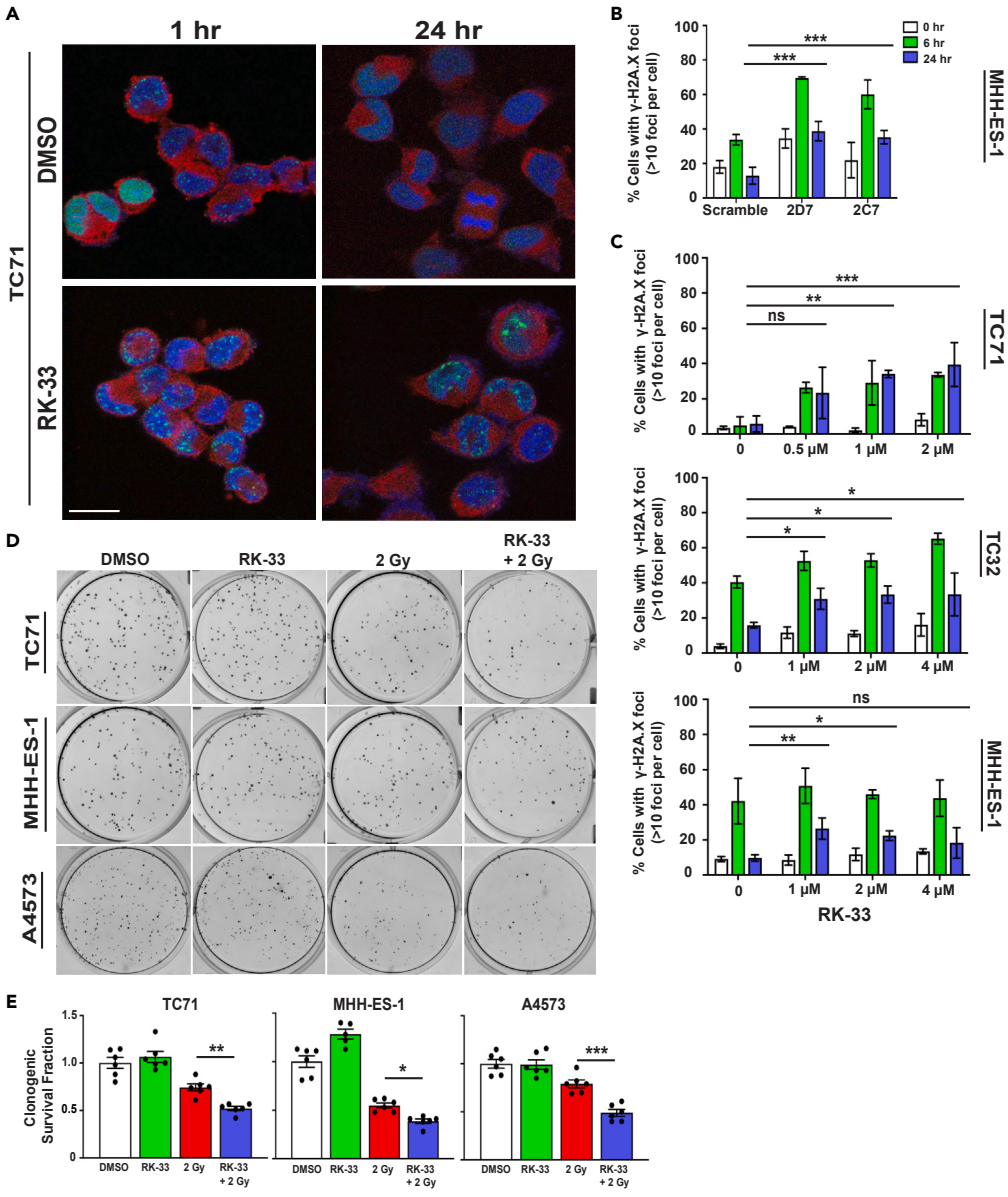

Figure 2. Inhibition of DDX3 radiosensitizes EWS

(A) Immunofluorescent images of TC71 EWS cells at 1 or 24 h following 2 Gy IR that were treated with either DMSO (top) or 2 μM RK-33 (bottom). Green = γ-H2A.X detection, marking double-stranded DNA breaks (DSB); Red = DDX3; Blue = DAPI stain. Mag bar: 20 μm.

(B) Quantitation of γ-H2A.X foci in stable genetically modified shDDX3 MHH-ES-1 cell lines 2D7 and 2C7 at 0 (i.e., no treatment), 6, and 24 h following 2 Gy IR. Data are representative of three independent experiments. Data are mean ± SD. *$p < 0.05$ and ***$p < 0.001$ determined by two-Way ANOVA followed by Šídák's multiple comparisons test.

(C) Quantitation of γ-H2A.X foci in three independent EWS cell lines (TC71, MHH-ES-1, and TC32) where cells were irradiated with 2 Gy in the presence of 0, 0.5, 1, 2, or 4 μM RK-33. Data represent three independent experiments per cell line. Data are mean ± SD. *$p < 0.05$ and ***$p < 0.001$ determined by two-Way ANOVA followed by Šídák's multiple comparisons test.

(D and E) TC71, MHH-ES-1, and A4573 EWS cells were treated with either DMSO, 2 Gy, 2 μM RK-33, or 2 μM RK-33 + 2 Gy and plated at densities of 200 or 400 cells/well 6 h post-IR. Cells were then grown in conditioned media for five days and stained with crystal violet for (D) visualization and (E) quantification of clonogenic survival fractions (n = 6 technical replicates per cohort per cell line). Results represent one experiment of three independent experiments per cell line. Data are mean ± SEM. *$p < 0.05$, **$p < 0.01$, and ***$p < 0.001$ determined by one-way ANOVA followed by Šídák's multiple comparisons test.

respectively express low (DDX3^{low}) and high (DDX3^{high}) levels of DDX3 protein (Figure 3A), were utilized to test whether RK-33 could act as a radiosensitizing agent when combined with sub-therapeutic doses of columnated IR (10 Gy; Figure 3B). Single-agent treatment with a sub-therapeutic dose of 50 mg/kg RK-33 ($p = 0.1777$) did not significantly alter tumor volume, whereas IR, alone ($p = 0.0095$) or in combination with

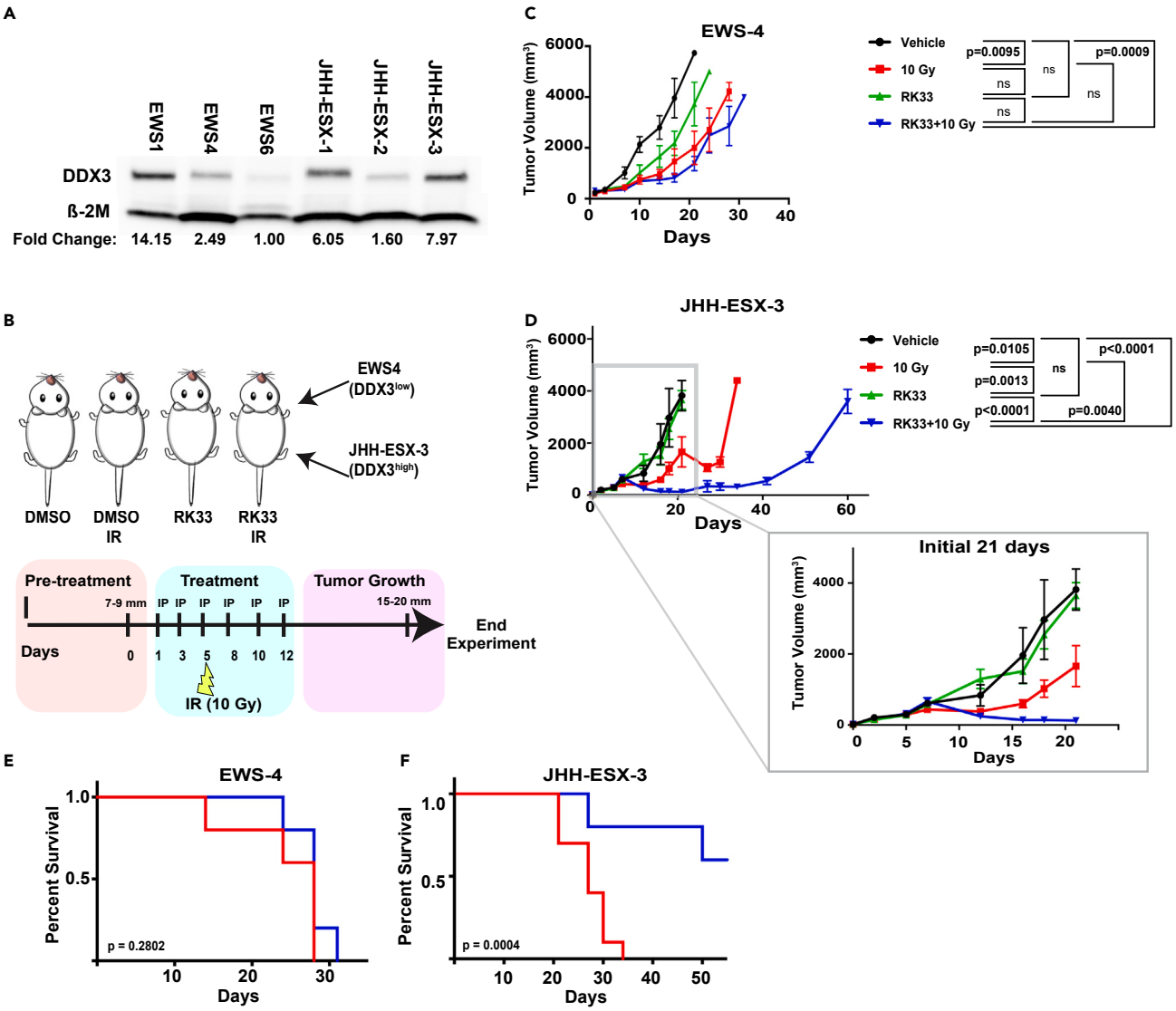

Figure 3. RK-33 induces radiosensitization in EWS xenograft models expressing high levels of DDX3

(A) Quantitation of DDX3 protein expression in six independent EWS PDX models. All samples were normalized using the corresponding loading control, β-2M. Fold changes of protein abundance were calculated by comparing normalized band densities to EWS6 abundance and are noted below each sample for comparison. β-2M = beta 2-microglobulin.

(B) Schematic representation of treatment schedule and cohorts of two independent EWS xenograft NSG mouse models: EWS4 (DDX3^{low}) and JHH-ESX-3 (DDX3^{high}). Tumor chunks were implanted subcutaneously. Upon reaching a tumor diameter of 7–9 mm, mice received every other day intraperitoneal (IP) injections of either DMSO or RK-33 (25 mg/kg) for two weeks, with radiation cohorts (IR) receiving 10 Gy IR administered 6 h following drug treatment on day 5. Mice were euthanized and tumors collected after growing to a diameter of 15–20 mm or day 60, whichever came first. Tumors were measured with calipers twice weekly.

(C and D) Tumor volumes of DDX3^{low} (C) and DDX3^{high} (D) were measured and calculated over a period of 29–60 days, respectively. Inset shows changes in DDX3^{high} tumor volume during the first 21 days post-treatment demonstrating tumor ablation of RK-33/10 Gy cohort by day 16. Results represent one experiment of 5–10 mice per cohort per PDX. Data are mean ± SEM. Statistical significance was determined by two-way mixed effects ANOVA followed by Tukey's multiple comparisons test.

(E and F) Kaplan-Meier curves demonstrating survival of 10 Gy versus RK-33/10 Gy cohorts of DDX3^{low} (E) and DDX3^{high} (F) PDXs. Statistical significance was determined by log rank (Mantel-Cox) test.

RK-33 ($p = 0.0009$), resulted in a significant decrease of volume in the DDX3^{low} PDX (Figure 3C). Importantly, the DDX3^{high} PDX was completely ablated ($p < 0.0001$) by combined DDX3 inhibition and IR as early as 10 days post-IR (Figure 3D inset), an effect that was maintained for several weeks before tumor recurrence (Figure 3D). Additionally, combination therapy of RK-33 with IR significantly improved the survival rate of mice implanted with DDX3^{high} ($p = 0.0004$) but not DDX3^{low} ($p = 0.2802$) EWS PDXs (Figures 3E and 3F), consistent with DDX3^{high} tumors having a

greater dependency on DDX3, as we have previously reported.[10] Taken together, these data demonstrate that the impact of RK-33 is dependent upon the level of expression of its target, DDX3, and provide support for the development of RK-33 as a radiosensitizing agent in EWS patients whose tumors demonstrate high levels of DDX3 protein expression.

Homologous and non-homologous DDR pathways are impaired by DDX3 inhibition

Recent studies suggest that EWS inherently has impaired homology-directed DNA damage repair (HR) owing to sequestration of BRCA1 by hyperphosphorylated RNAPII via an EWS-FLI1-dependent mechanism.[18] Therefore, we hypothesized that RK-33 inhibition of DDX3 in EWS could further exacerbate the tumor's basal impaired ability to repair genomic damage, resulting in enhanced persistence of double-stranded DNA breaks, thus contributing to the pronounced *in vivo* radiosensitization phenotype. To determine which DDR pathways were affected by DDX3 abrogation, we utilized I-SceI GFP reporter constructs in U2OS cells[19,20] to identify and quantify double-stranded DNA break repair mechanisms including HR and total end joining, which is reflective of non-homologous end joining (NHEJ). These reporters consist of two non-functional GFP genes in tandem. The upstream gene has a mutation introducing the I-SceI recognition site, and the downstream gene is an internal fragment. Upon induction of an I-SceI double-strand break, the downstream gene operates as a template to repair the break when HR or NHEJ is proficient, resulting in functional GFP gene expression that can be measured by flow cytometry. Knockdown of DDX3 (Figure 4A) resulted in a significant decrease in both HR ($p < 0.001$) and NHEJ activity ($p < 0.001$) as measured by this assay (Figure 4B). In contrast, single-strand annealing DNA repair was unaffected with DDX3 impairment (Figure 4B). These data suggest a role for DDX3 in both homologous and non-homologous double-stranded DNA break repair.

Repair of double-stranded DNA breaks (DSB), either through HR or NHEJ, involves multiple proteins and signaling cascades that direct the repair pathways.[21] Given the role of DDX3 in translational regulation,[22–24] we began to investigate how DDX3 inhibition impairs DDR by assessing changes in protein abundance and signaling following RK-33 treatment of EWS cells with or without IR. TC71 or MHH-ES-1 cells were pre-treated with either DMSO or RK-33 for 1 h prior to receiving 2 Gy IR. Cells were collected for protein analysis at either 1 or 24 h post-IR. Western blots were performed assessing a panel of proteins involved with DSB repair (DSBR) (Figure S1) (n = 2–3 experiments per cell line). We did not observe any consistent modulations in the abundance of proteins involved in either the HR or NHEJ repair pathways. Aside from gamma phosphorylation of H2A.X, no gross alterations in DDR signaling were observed with RK-33 treatment following IR, such as the phosphorylation of BRCA1 at Ser1423.[25,26] Neither did we find evidence of RK-33 altering CHK1 Ser345 phosphorylation or replication protein A subunit 32 (RPA32) on Ser4/Ser8, markers for replication fork stress.[27,28] These data suggest that DDX3 does not regulate DSBR by grossly altering the abundance or signaling cascades of proteins involved in DSBR or replication stress.

DDX3 associates with HR proteins but not at sites of double-stranded DNA breaks

We next investigated whether DDX3 might physically interact with proteins of the HR and NHEJ repair pathways. Immunoprecipitations of DDX3 were performed and analyzed via western blot for a panel of DDR proteins involved in HR and/or NHEJ repair (Figure 4C). Proteins associated with NHEJ repair, such as Ku70 and Ku86 (reviewed in[29]) did not interact with DDX3, whereas ATP-dependent DNA helicase Q1 (RECQL1), RPA32, DNA repair protein RAD51 homolog 1 (RAD51), and X-ray repair cross-complementing 2 (XRCC2) (reviewed in[21,30,31]), all of which contribute to homology-directed repair, co-immunoprecipitated with DDX3 in three independent EWS cell lines (Figures 4C and S2A).

Given the observation that DDX3 interacts with several DNA repair proteins, but these DDR proteins are generally considered to be localized to the nucleus while DDX3 can have both cytoplasmic and nuclear distribution, we evaluated the subcellular localization of these proteins. As expected, DDX3 was present in both the nuclear and cytoplasmic fractions. Interestingly, DDX3 DDR interacting proteins, RPA32, RAD51, XRCC2, and, to a lesser extent, RECQL1, were found not only in the nuclear fraction but also in the cytoplasm (Figures 4D and S2B); eIF4E, H2A.X, and NUP205 provide controls for the quality of the fractionation. By immunofluorescence we did not observe any DDX3 colocalization at sites of DSBs, as identified by the presence of γ-H2A.X foci (Figure 4E). These data suggest that endogenous DDX3 does not directly contribute to DSBR at the site of DNA damage but possibly through interactions with DDR proteins in the cytoplasm of EWS cells.

RNA helicase DDX3 interacts with cytoplasmic oligonucleotide substrates in EWS

Successful DDR relies on regulated translocation of several DDR proteins from the cytoplasm to the nucleus in response to DNA damage, as has been previously investigated with BRCA1-, BRCA2-, and BRCA1-associated RING domain protein 1 (BARD1), TP53-binding protein 1 (53BP1), BRCA1-associated ATM activator 1 (BRAT1), exonuclease 1 (EXO1), XRCC4, and RAD51.[32–37] Considering that (1) DDX3 localization in EWS is both nuclear and cytoplasmic, (2) endogenous DDX3 does not localize to sites of DSBs, and (3) DDX3 interacts with HR proteins, we hypothesized that impairment of DDX3 helicase activity could sequester DDX3, and potentially DDR proteins, in the cytoplasm, thus preventing appropriate translocation into the nucleus, resulting in an inhibition of DDR.

Recent studies have demonstrated replication stress in EWS that appears to be driven by the EWS-FLI1 fusion protein.[18,38,39] More specifically, EWS-FLI1 expression causes hyperphosphorylation of RNAPII, increasing transcription and resulting in increased R-loop abundance, replication stress, and DNA damage.[18] High levels of DNA replication stress have also been associated with cytoplasmic accumulation of genomic DNA (reviewed in[40]). Based on this concept, we looked for cytoplasmic DNA and noted its presence as well as micronuclei in multiple EWS cell lines, EWS PDXs, and EWS patient samples (Figures 5A–5C). Additionally, DDX3 has been shown to interact with multiple oligonucleotide substrates *in vitro*, including RNA:RNA duplexes, RNA:DNA hybrids, and single-stranded DNA, with decreasing affinity respectively.[22,41] Given this, we looked to determine if these different forms of nucleic acid structures were present in the cytoplasm of EWS cells.

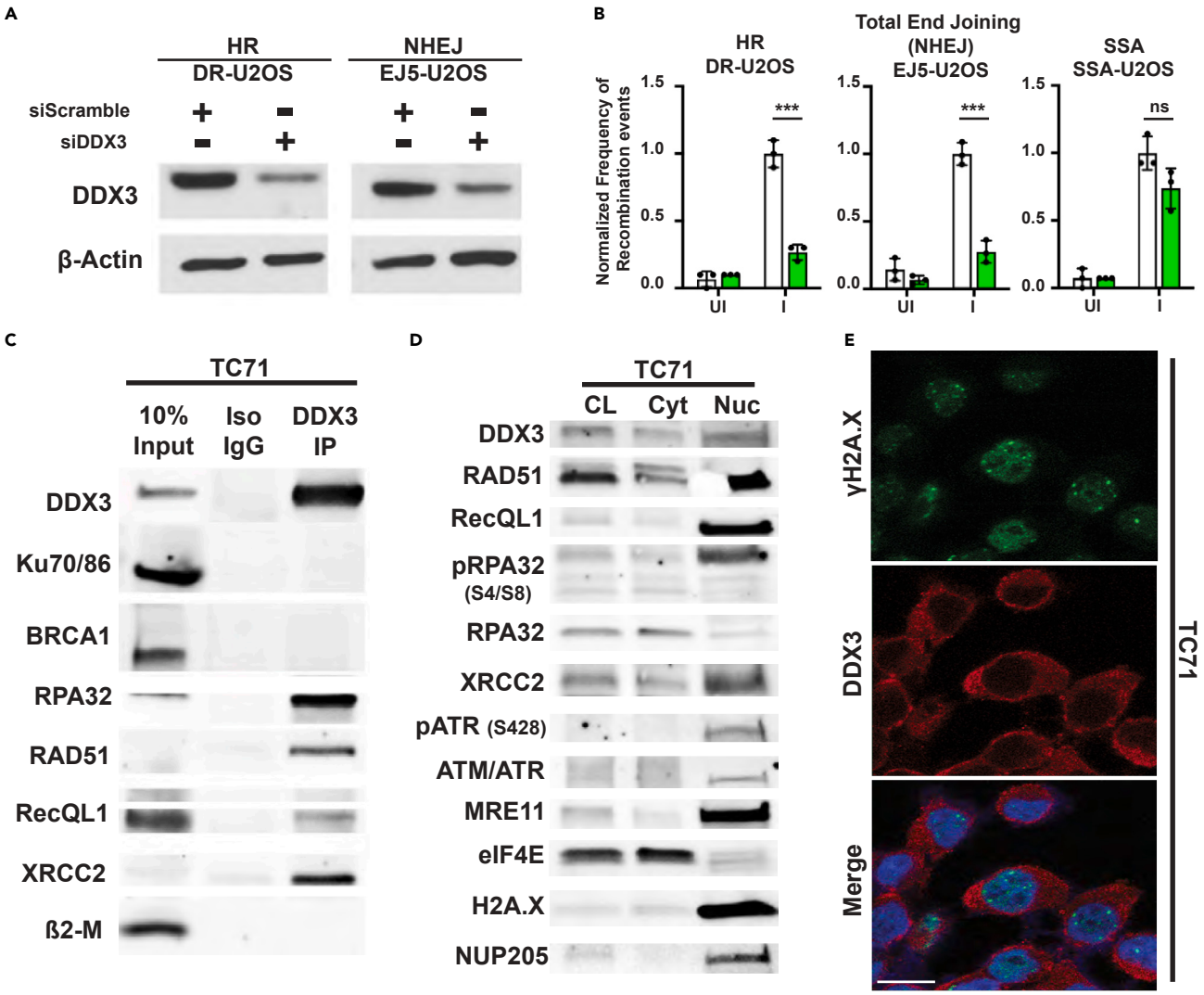

Figure 4. DDX3 interacts with components of the homologous DDR pathway

(A) Western blots of DR-U2OS and EJ5-U2OS cell lysates following siRNA knockdown of DDX3.

(B) DR-U2OS, EJ5-U2OS, and SSA-U2OS cell lines were treated with either scramble or siDDX3 and then transfected with the I*Sce*I-pCAGGS vector or an empty vector to induce DNA damage. Effective DDR was visualized by induction of GFP expression and quantified using flow cytometry. Results represent three independent experiments per cell line. Data represent frequency of DNA recombination events ±SEM. ***$p < 0.001$ determined by multiple unpaired t tests followed by Šídák's multiple comparisons test. I, induction of DNA damage with I*Sce*I-pCAGGS; UI, non-induction with empty pCAGGS vector; HR, homologous recombination; NHEJ, non-homologous end-joining; SSA, single-strand annealing.

(C) Immunoprecipitation (IP) of TC71 EWS cell lysates using anti-DDX3 antibodies conjugated to magnetic beads. Western blots demonstrate co-immunoprecipitation of various DDR proteins with endogenous DDX3. Iso IgG, immunoprecipitation of TC71 cell lysates using control isotype antibodies. Results are representative of three independent experiments. See also Figure S2.

(D) Subcellular fractionations of TC71 cells demonstrate the presence of DDX3, RAD51, RECQL1, RPA32, and XRCC2 in both cytoplasmic and nuclear compartments. Results are representative of three independent experiments. See also Figure S2. CL, whole-cell lysate.

(E) Immunofluorescent images of TC71 EWS cells 6 h after treatment with 5 μM RK-33 and 2 Gy IR. Green = γ-H2A.X staining of double-stranded DNA breaks (DSB); Red = DDX3; Blue = DAPI stain. Mag bar: 20 μm.

Intriguingly, we discovered that both single-stranded DNA (ssDNA) and RNA:DNA hybrid structures are present in the cytoplasm of EWS cells with the majority of cytoplasmic ssDNA substrates colocalizing with RNA:DNA hybrids (Figure 5D). Indeed, cytoplasmic S9.6 staining was consistently observed in EWS but not in primary umbilical cord-derived mesenchymal stem cells (Figure 5E), suggesting that increased cytoplasmic RNA:DNA hybrid structures is a sequela of oncogenic transformation in EWS. We confirmed the identity of the cytoplasmic RNA:DNA hybrid structures by overexpressing RNaseH1, an *in vitro* technique commonly used to resolve nuclear RNA:DNA hybrid structures, such as transcriptional R-loops, by specifically degrading the RNA strand.[42–44] Lentivirus-driven overexpression of $RNaseH1^{WT}$ in EWS cell lines

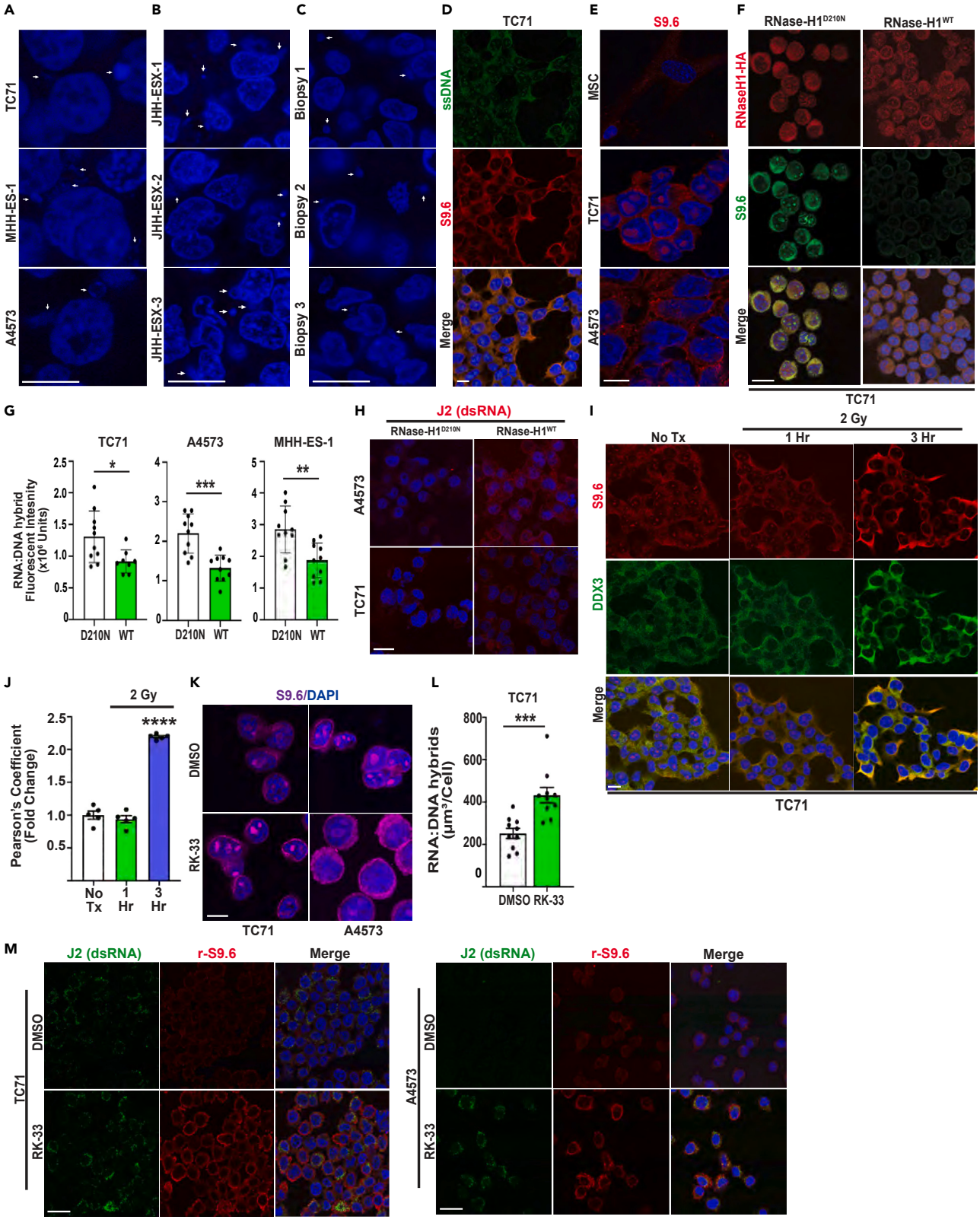
A
TC71
MHH-ES-1
A4573
B
JHH-ESX-1
JHH-ESX-2
JHH-ESX-3
C
Biopsy 1
Biopsy 2
Biopsy 3
D
TC71
ssDNA
S9.6
Merge
E
S9.6
MSC
TC71
A4573
F
RNase-H1D210N
RNase-H1WT
RNaseH1-HA
S9.6
Merge
TC71
G
TC71
A4573
MHH-ES-1
RNA:DNA hybrid Fluorescent Intesnity (x10⁶ Units)
D210N WT
H
J2 (dsRNA)
RNase-H1D210N
RNase-H1WT
A4573
TC71
I
2 Gy
No Tx
1 Hr
3 Hr
S9.6
DDX3
Merge
TC71
J
2 Gy
Pearson's Coefficient (Fold Change)
No Tx
1 Hr
3 Hr
K
S9.6/DAPI
DMSO
RK-33
TC71
A4573
L
TC71
RNA:DNA hybrids (μm³/Cell)
DMSO RK-33
M
J2 (dsRNA)
r-S9.6
Merge
TC71
DMSO
RK-33
A4573
DMSO
RK-33

Figure 5. DDX3 interacts with and modulates cytoplasmic oligonucleotide substrates in EWS

(A–C) DAPI staining of dsDNA in three independent EWS cell lines (A), three independent xenografts (B), and three independent patient samples (C). White arrows show examples of extra-nuclear dsDNA substrates. Mag bars: 10 μm.

(D) Immunofluorescent images of TC71 EWS cells. Data are representative of two independent experiments. Green = single-stranded DNA (ssDNA); Red = RNA:DNA hybrid structures; Blue = DAPI stain. Mag bar: 24 μm.

(E) Representative images of S9.6 staining of umbilical-cord-derived human mesenchymal stem cells (MSC), TC71, and A4573 EWS cell lines. Mag bar: 10 μm.

(F and G) Three independent EWS cell lines, TC71, A4573, and MHH-ES-1, were transduced with lentivirus overexpressing either RNaseH1^{WT} or enzymatically dead RNaseH1^{D210N} for 48 h. Cells were then stained, and immunofluorescent (IF) confocal images were obtained (F) and basal RNA:DNA hybrid abundance quantified (G). Results are representative of four to five high power field (hpf) per condition from two independent experiments per cell line. Data represent mean fluorescent intensity per cell per hpf +/− SEM. *p < 0.05, **p < 0.01, and ***p < 0.001 determined by unpaired t tests. Red = HA-tag; Green = RNA:DNA hybrids (S9.6 staining); Blue = DAPI stain. Mag bar: 10 μm.

(H) TC71 and A4573 EWS cell lines were transduced with either RNaseH1^{WT} or enzymatically dead RNaseH1^{D210N} for 48 h. Cells were then stained with J2 to visualize dsRNA. Representative IF confocal images are shown. Mag bar: 10 μm.

(I and J) Representative IF images of TC71 cells at 1 and 3 h post-2 Gy IR (I). Colocalization of DDX3 and RNA:DNA hybrid fluorescence was analyzed and quantified using Pearson's coefficient. Data are representative of five high power fields (hpf) per cohort from one of three independent experiments (J). Data are mean ± SEM. ****p < 0.0001 determined by one-way ANOVA followed by Dunnett's multiple comparisons test. Green = DDX3; Red = RNA:DNA hybrid structures; Blue = DAPI stain. Mag bar: 24 μm.

(K and L) TC71 and A4573 cells were treated with either vehicle control (DMSO) or 2 μM RK-33. Immunofluorescent z stack confocal images were obtained (K). TC71 images were measured for volume of RNA:DNA hybrid structures per cell (L). Results are representative of five hpf per condition from two independent experiments. Data represent mean fluorescent intensity per cell +/− SEM. ***p < 0.001 determined by unpaired t test. Mag bar: 10 μm.

(M) Representative double-stained IF images analyzing RNA:DNA hybrid and double-stranded RNA (dsRNA) distribution with a rabbit-S9.6 and J2 antibodies, respectively, in TC71 and A4573 EWS cell lines treated with either DMSO or 2 μM RK-33. Mag bar: 10 μm.

significantly reduced cytoplasmic RNA:DNA hybrid abundance, as demonstrated by S9.6 antibody staining,[45] compared with the enzymatically inactive mutant RNaseH1^{D210N}[46] (Figures 5F and 5G). Conversely, cytoplasmic RNA:RNA duplexes, identified with the J2 antibody specific for dsRNA,[47] increased following RNaseH1^{WT} overexpression (Figure 5H), which is consistent with dissociated RNA from RNA:DNA hybrids forming secondary and tertiary structures. Importantly, cytoplasmic J2 staining was minimal in EWS overexpressing the RNaseH1^{D210N} control (Figure 5H), suggesting that dsRNA is less likely the nucleic acid substrate responsible for the cytoplasmic localization of DDX3. Next, we examined whether DDX3 colocalized with cytoplasmic RNA:DNA hybrids or with ssDNA. Although DDX3 colocalized with both substrates, DDX3 demonstrated a more robust colocalization with cytoplasmic RNA:DNA hybrids (Figure 5I) compared with ssDNA under basal conditions (Figure S3). Together, these findings suggest that DDX3 preferentially interacts with cytoplasmic RNA:DNA oligonucleotide substrates in EWS, which could account for the cytoplasmic localization of DDX3.

To query whether the interaction of DDX3 with cytoplasmic RNA:DNA hybrids could contribute to the radiosensitization effect of RK-33 in EWS, we treated EWS cell lines with 2 Gy IR and examined changes in the interactions between DDX3 and RNA:DNA hybrid substrates. DDX3 co-localization with cytoplasmic RNA:DNA hybrid structures significantly increased in a time-dependent manner following IR ($p < 0.0001$; Figures 5I and 5J), suggesting that IR damage increases the interaction of DDX3 with cytoplasmic RNA:DNA hybrids.

Inhibition of DDX3 helicase activity by RK-33 impairs resolution of cytoplasmic RNA:DNA hybrid structures

DDX3 is an ATP-dependent DEAD-box RNA helicase that resolves oligonucleotide duplexes in a non-processive manner.[6] The DDX3 inhibitor, RK-33, specifically binds to the catalytic pocket of the DDX3 ATPase catalytic domain, thus inhibiting helicase activity and preventing the resolution of oligonucleotide duplexes.[11,12] Thus, we hypothesized that impairment of DDX3 RNA helicase activity by RK-33 should result in an increase of hybrid structures. Indeed, when EWS cell lines were treated with RK-33 alone, S9.6 staining of cytoplasmic RNA:DNA hybrid structures significantly increased ($p = 0.0007$; Figures 5K and 5L). We confirmed that the increased cytoplasmic staining with S9.6 reflects an increase in RNA:DNA hybrids and not an increase in dsRNA by co-staining EWS cell lines with the dsRNA-specific murine J2 antibody and the rabbit-derived S9.6 antibody (Figure 5M). The rabbit S9.6 antibody demonstrated a similar increase in cytoplasmic staining pattern in both TC71 and A4573 cell lines, as demonstrated using the murine hybridoma S9.6 antibody (Figure 5K), in response to RK-33 treatment (Figure 5M). Despite increased dsRNA staining following DDX3 inhibition, the J2 staining showed little to no co-localization with S9.6 moieties. Collectively, these data confirm that cytoplasmic RNA:DNA hybrids are present in EWS and demonstrate that inhibition of DDX3 RNA helicase activity attenuates the resolution of cytoplasmic RNA:DNA hybrid structures, thus increasing their abundance.

DDX3 inhibition by RK-33 sequesters RAD51 in the cytoplasm following IR

Our data support the hypothesis that RNA:DNA hybrid structures provide a cytoplasmic scaffold for DDX3 in EWS and that impairing the helicase activity of DDX3 with RK-33 further enhances this cytoplasmic localization. We next tested whether the cytoplasmic localization of DDX3 contributes to the radiosensitizing effect of RK-33. As described earlier, the HR proteins RAD51, RPA32, RECQL1, and XRCC2, which co-immunoprecipitate with DDX3 (Figure 4C), were also observed in the cytoplasmic fraction of two independent EWS cell lines (Figures 4D and S2B). The importance of subcellular localization and its effect on DDR of only one of these four candidate DDR proteins, RAD51, has been well characterized.[32,48–51] Accurate repair of damaged DNA depends on the proper localization of RAD51 to sites of dsDNA breaks following IR-induced damage.[52] Additionally, RAD51 depletion impairs RAD51 loading in both homologous DDR and the resolution of stalled replication forks.[52] In both cases, single-stranded regions of DNA are then exposed to exonucleases, which ultimately result in increased genomic

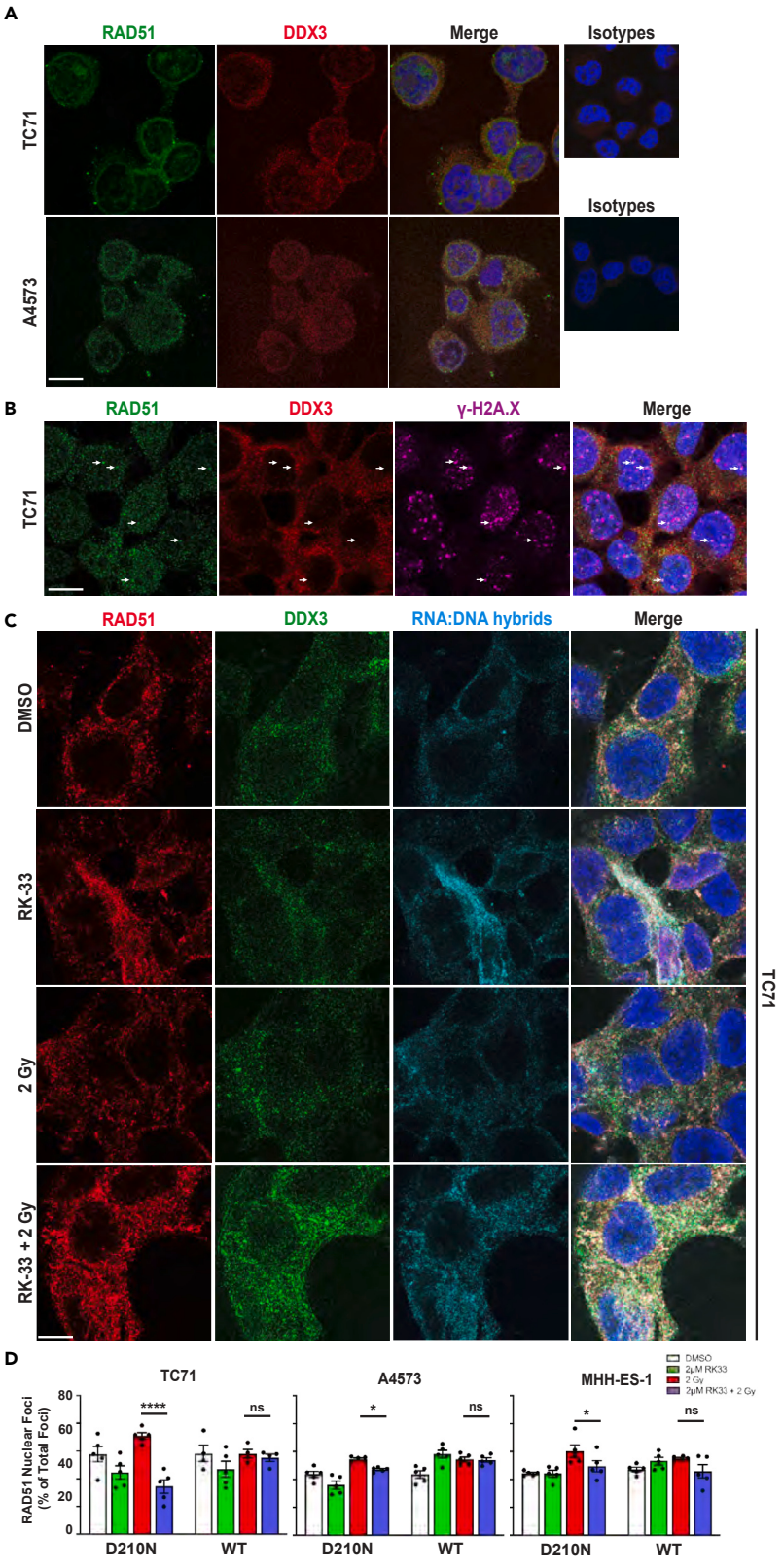
A
RAD51
DDX3
Merge
Isotypes
TC71
Isotypes
A4573
B
RAD51
DDX3
γ-H2A.X
Merge
TC71
C
RAD51
DDX3
RNA:DNA hybrids
Merge
DMSO
RK-33
2 Gy
RK-33 + 2 Gy
TC71
D
TC71
A4573
MHH-ES-1
DMSO
2μM RK33
2 Gy
2μM RK33 + 2 Gy
RAD51 Nuclear Foci (% of Total Foci)
80
60
40
20
0
****
ns
*
ns
*
ns
D210N
WT
D210N
WT
D210N
WT

Figure 6. Inhibition of DDX3 helicase activity sequesters RAD51 in the cytoplasm in an RNA:DNA-hybrid-dependent manner following IR

(A) Representative immunofluorescent images of two EWS cell lines, TC71 and A4573, demonstrating cytoplasmic colocalization of endogenous RAD51 (green) and DDX3 (red) at basal levels. Data are representative of three independent experiments. Blue = DAPI stain. Mag bar: 10 μm.

(B) Representative immunofluorescent images of TC71 cells demonstrating colocalization of RAD51 (green) with DSBs, evidenced by γ-H2A.X (purple) staining, 3 h following 2 Gy IR. Data are representative of two independent experiments. Red = DDX3; Blue = DAPI stain. Mag bar: 10 μm.

(C) Immunofluorescent images of TC71 cells at 3 h following treatment with either DMSO (top), 2 μm RK-33 (second row), DMSO +2 Gy IR (third row), or 2 μM RK-33 + 2 Gy (bottom). Data are representative of three independent experiments. Green = DDX3; Red = RAD51; Cyan = RNA:DNA hybrids; Blue = DAPI stain. Mag bar: 20 μm.

(D) Three independent EWS cell lines, TC71, A4573, and MHH-ES-1, were transduced with lentivirus overexpressing either RNaseH1^{WT} or enzymatically dead RNaseH1^{D210N} for 48 h prior to performing radiosensitization assays. Cells were stained and immunofluorescent, z-stacked confocal images were obtained. RAD51 foci were quantified for each experimental cohort. Results represent nuclear RAD51 foci as a percentage of total RAD51 foci from all Z-planes of 4–5 representative hpf from each experimental cohort of each cell line. Data represent one of three independent experiments. Data are mean ± SEM. *$p < 0.05$ and ***$p < 0.001$ determined by two-way ANOVA followed by Šídák's multiple comparisons test.

instability and accumulation of cytoplasmic self-DNA.[52,53] Considering that EWS has high basal levels of R-loops, replication stress,[18] and cytoplasmic oligonucleotide structures (Figures 5A–5C), we examined whether DDX3 helicase impairment also altered RAD51 cellular localization, providing a mechanistic explanation for our observation that RK-33 acts as a radiosensitizing agent.

Under basal conditions, RAD51 localizes to both the cytoplasm and nucleus and partially colocalizes with DDX3 in the cytoplasm in TC71 and A4573 EWS cells (Figure 6A). Within 4 h of IR (2 Gy), distinct RAD51 nuclear foci were observed, which localized with nuclear γ-H2A.X foci, whereas DDX3 did not (Figure 6B). In contrast, when DDX3 helicase activity was inhibited by RK-33, IR-induced RAD51 focus formation was diminished and pronounced RAD51 colocalization with cytoplasmic DDX3, and RNA:DNA hybrids was observed (Figure 6C). Growing evidence suggests that RNA:DNA hybrids form at sites of DSBs and play a role in DDR.[54–57] Additionally, the presence of RNA:DNA hybrids has been associated with recruitment of RAD51 to sites of DSBs.[55–57] Therefore, we explored whether the increase of cytoplasmic RNA:DNA hybrids following IR and DDX3 helicase inhibition may be sequestering RAD51 in the cytoplasm. To test this, we overexpressed RNaseH1^{WT} in three independent EWS cell lines to resolve cytoplasmic RNA:DNA hybrids and then quantified nuclear RAD51 foci following RK-33 treatment. If RAD51 is sequestered in the cytoplasm, we hypothesized that the percentage of total cellular RAD51 foci that is nuclear should decrease. In cells expressing the RNaseH1^{D210N} enzymatically inactive control, RAD51 foci increased with IR alone (Figure 6D) as expected from our data demonstrating IR-induced nuclear and cytoplasmic RAD51 foci formation (Figures 6B and 6C). Moreover, when RNaseH1^{D210N}-expressing EWS cells were treated with both IR and RK-33, which increases cytoplasmic RNA:DNA hybrid structures, there was a significant decrease in nuclear RAD51 foci compared with cells treated only with IR in three independent EWS cell lines (Figure 6D – red vs. blue bars). Importantly, when cytoplasmic RNA:DNA hybrids were resolved by overexpression of RNaseH1^{WT} (Figure 5F), RK-33 treatment combined with IR was unable to significantly alter the nuclear formation of RAD51 foci (Figure 6D—red vs. blue bars), suggesting that removal of the cytoplasmic RNA:DNA hybrid scaffolds allowed nuclear localization of RAD51. These findings support our hypothesis that impairment of DDX3 helicase function, via RK-33, prevents resolution of DSBs induced by IR by sequestering RAD51 in the cytoplasm and preventing formation of nuclear foci at the site of DSBs through a mechanism that is dependent on modulation of cytoplasmic RNA:DNA hybrid structures.

DISCUSSION

In this study, we elucidate a novel mechanism of radiosensitization for the therapeutic targeting of cancers that accumulate cytoplasmic nucleic acid structures that arise in tumors with high levels of replication stress, like EWS. To our knowledge, we are the first to demonstrate that altering cytoplasmic RNA:DNA hybrid abundance via inhibition of a DEAD-box RNA helicase abrogates the repair of IR-induced DSBs by cytoplasmic sequestration of an essential DDR protein, thereby impeding DNA repair following radiotherapy (Figure 7). Inhibition of DDX3 helicase activity, using RK-33, increased cytoplasmic RNA:DNA hybrid structures. When RK-33 was combined with IR, RAD51 was sequestered in the cytoplasm and colocalized with cytoplasmic RNA:DNA hybrids, thereby reducing the formation of nuclear RAD51 foci required for HR of DSBs. Whether the increased cytoplasmic RAD51 abundance occurred from RAD51 binding to excised nuclear RNA:DNA hybrid structures before exportation out of the nucleus or from *de novo* binding to cytoplasmic RNA:DNA scaffolds, the sequestration phenotype was reversed following removal of RNA:DNA hybrid structures, thus demonstrating a role for these structures in DDR. Our data suggest that leveraging the by-products of increased replication stress, i.e., cytoplasmic RNA:DNA hybrid structures, as scaffolds for DDR protein sequestration could provide a novel and viable therapeutic approach for targeting cancers characterized by high levels of replication stress.

Accumulation of cytoplasmic self-DNA structures is one of the many cellular sequelae of neoplastic hyperproliferation, i.e., oncogene-induced replication stress (reviewed in[58]), which is characteristic of EWS biology.[18,59] We confirmed that not only cytoplasmic DNA substrates, but also ssDNA and RNA:DNA hybrid structures, are present in EWS cell lines and PDX models, as well as in primary human EWS samples. Indeed, ssDNA and RNA:DNA hybrid structures were present in both the nucleus and cytoplasm. These findings are in line with current studies reporting that EWS-FLI1 increases transcriptional R-loops in EWS and that cytoplasmic RNA-DNA hybrid structures increase as a result of increased nuclear R-loop processing.[18,59] We demonstrated a robust association between DDX3 and the cytoplasmic RNA:DNA hybrid structures compared with ssDNA substrates. Several studies have implicated DDX3 in cellular pathways that regulate cytoplasmic oligonucleotide moieties. DDX3 has been shown to act as a sensor of cytoplasmic ssRNA and dsRNA through the RIG-1 (retinoic acid-inducible

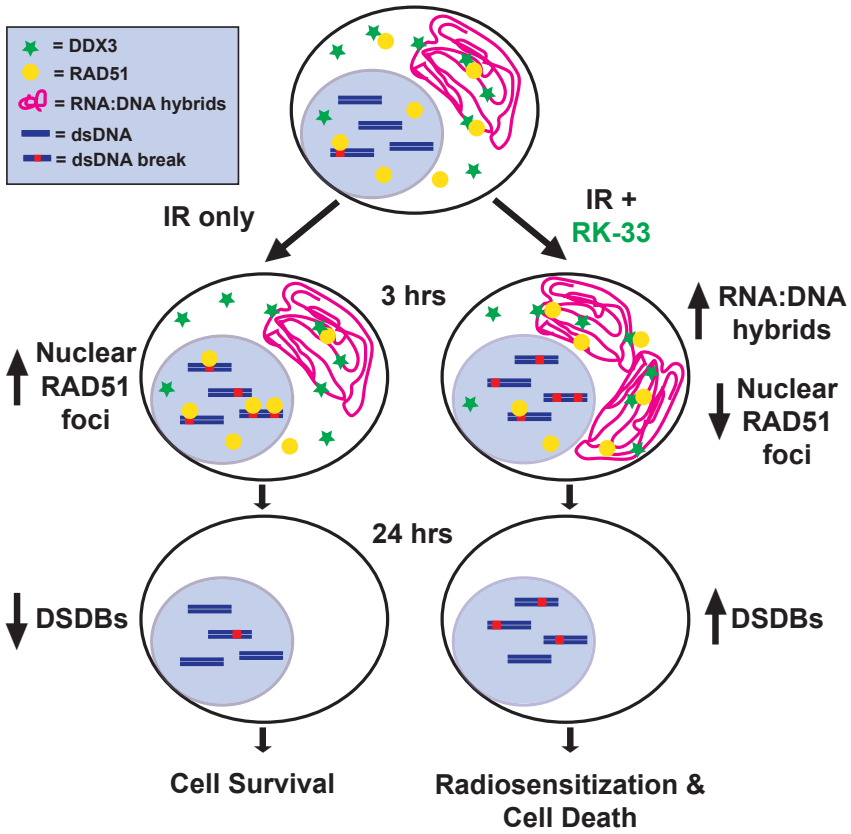

Figure 7. Mechanistic model of Ewing sarcoma radiosensatization following DDX3 RNA helicase inhibition

EWS's genomic instability is evidenced by basal levels of double-stranded DNA breaks (DSBs) and cytoplasmic RNA:DNA hybrid structures. Endogenous DDX3 associates with both cytoplasmic RNA:DNA hybrids and RAD51. When ES is subjected to IR, RAD51 foci form at sites of IR-induced DSBs within 3 h. Within 24 h, the majority of DSBs are resolved back to basal levels, resulting in cell survival. In contrast, inhibition of DDX3 RNA helicase activity, with RK-33, impairs resolution and increases the abundance of cytoplasmic RNA:DNA hybrid structures. RAD51 is sequestered in the cytoplasm in an RNA:DNA-hybrid-dependent manner and results in decreased nuclear foci formation, thereby impairing HR of IR-induced DSBs. The resultant radiosensitization significantly impairs cell survival over IR therapy alone.

gene 1)/MAVS (mitochondrial antiviral signaling protein) signaling pathwaythat activates IKKε (IκB kinase-ε)/IRF3 (interferon regulatory factor 3) signaling to induce a type 1 interferon response.[60–63] Roles for DDX3 have also been described in the innate immunity pathways involving the NF-κB (nuclear factor κB) pathway through IKKβ,[64] the Toll-like receptor 7/8 signaling through NIK (NF-κB-inducing kinase)/IKKα, and alternative NF-κB signaling pathways.[65] A new study suggests that impairing the helicase activity of DDX3 results in a cytoplasmic accumulation of dsRNA, activating a dsRNA-sensing pathway through MDA5 (melanoma-differentiation-associated gene 5) signaling to induce an intrinsic type 1 interferon response in breast cancer.[66] Additionally, to rule out the involvement of one of two major cytoplasmic nucleotide sensing systems, the cGAS-STING[67] and TLR9[68] pathways, we examined whether cGAS localized with cytoplasmic RNA:DNA hybrids in our EWS cell lines and found that cGAS was predominantly localized to the nucleus via both immunofluorescent and subcellular fractionation studies (unpublished data), thus suggesting that the canonical cGAS-STING pathway is unlikely to be involved with DDX3 regulation of cytoplasmic RNA:DNA hybrids. Importantly, our findings expand the biological spectrum of cytoplasmic DDX3 function to include regulation of RNA:DNA hybrid structures. Our data indicate that DDX3 RNA helicase activity modulates and resolves cytoplasmic RNA:DNA hybrid structures *in vivo* in tumors with high levels of replication stress. In the context of IR, both RNA:DNA hybrid abundance and DDX3 localization to cytoplasmic hybrid structures increased in a time-dependent manner, whereas RK-33 impairment of DDX3 helicase activity further amplified the abundance of cytoplasmic RNA:DNA hybrids. This increase in RNA:DNA hybrid structures provided a cytoplasmic scaffold for sequestering the DDR protein RAD51.

These findings are based on immunofluorescent analysis of cytoplasmic oligonucleotides using antibody S9.6, which detects RNA:DNA hybrids, and J2, which binds dsRNA. There are reports in the literature suggesting S9.6 may not be specific for RNA:DNA hybrids and may, in fact, also recognize dsRNA in formalin fixed cells. In our cell lines and under our experimental conditions, it appears that S9.6 and J2 detect different substrates, with minimal cross-reactivity of S9.6. Evidence for this includes (1) the ability of wild-type, but not catalytically inactive, RNase-H1 to eliminate the S9.6 substrate (Figure 5F), (2) the inability of wild-type RNase-H1 to eliminate the J2 substrate (Figure 5H), and (3) the lack of overlap of the murine J2 and rabbit S9.6 immunofluorescence signals in co-immunofluorescence experiments (Figure 5M).

This constellation of results is most consistent with our contention that EWS cell lines accumulate cytoplasmic RNA:DNA hybrids and support our model that DDX3 regulates the abundance of cytoplasmic RNA:DNA hybrids, regulating the subcellular localization of RAD51.

Mounting evidence supports the importance of cellular localization of DDR proteins in preserving or impairing genomic stability.[32–37,48–51,69,70] Indeed, cytoplasmic sequestration of DDR proteins is an emerging therapeutic approach for cancer patients. Of note, previous studies revealed that lapatinib, an epidermal growth factor receptor (EGFR) inhibitor, induced a cytoplasmic localization of both BRCA1 and EGFR in triple-negative breast cancer models. This cytoplasmic sequestration resulted in a synthetic lethality when combined with a PARP inhibitor.[70] Leveraging this cytoplasmic sequestration phenomenon, a Phase 1 clinical trial was designed for patients with metastatic triple-negative breast cancer (NCT02158507), which demonstrated "promising antitumor activity" in the enrolled patients.[71] Other groups have implicated cytoplasmic sequestration of RAD51 in contributing to genomic instability and impaired DNA-damage repair through mechanisms involving AKT1 signaling,[32] IGF-R1 signaling,[50] and hexavalent chromium.[72] We discovered a novel mechanism for the cytoplasmic sequestration of DDR proteins where DDX3 helicase inhibition sequesters RAD51 predominantly in the cytoplasm, reduces the formation of nuclear RAD51 foci, and thus prevents RAD51 from participating in the nuclear repair of dsDNA breaks following IR. Our findings align with a recent study that also demonstrated impairment of nuclear RAD51 focus formation in sarcomas with high levels of HR deficiency.[73] Importantly, when we tested this therapeutic approach *in vivo* (Figure 3), pronounced tumor ablation resulted, which was maintained for several weeks. Therefore, our pre-clinical data suggest that physically altering the cellular localization of DDR proteins, such as RAD51, is a novel way to potentiate the effectiveness of radiation therapy, a critical treatment modality for many cancer patients.

The RNA helicase DDX3, which our data show plays a pivotal role in regulating the subcellular localization of RAD51, has been studied in multiple adult and pediatric cancers.[7,12,23,74–77] The role of DDX3 in these cancers is context-dependent, acting as either an oncogene or a tumor suppressor depending on the cancer and even cancer sub-types (reviewed by[23]). Previously, we have demonstrated that DDX3 functions as an oncogene in EWS.[10] Here, we demonstrate that 75% of EWS tumors examined express moderate to high levels of DDX3 and that high levels of DDX3 expression are associated with poor survival. These findings, in combination with our previous work, strongly implicate the RNA helicase DDX3 as a therapeutic target for EWS patients.

EWS patients with recurrent, metastatic, and unresectable disease currently have poor prognoses for long-term survival.[1,2] Considering that radiation therapy is commonly used to treat these patients,[14,15] our finding that the DDX3 RNA helicase inhibitor, RK-33, functions as a radiosensitizing agent is particularly important. We found that DDX3 inhibition, both genetically and chemically, sensitizes EWS to IR-induced cell death by delaying the repair of IR-induced DSBs in multiple EWS cell lines. Clonogenic survival of EWS cells was impaired compared with IR or RK-33 alone *in vitro* when treated with 2 μm RK-33 and 2 Gy IR. In agreement with these findings, a pronounced *in vivo* tumor ablation occurred following RK-33 radiosensitization in a $DDX3^{high}$ EWS PDX model, thus demonstrating the clinical potential for RK-33 as a radiosensitizing agent for EWS patients. Of note, from the $DDX3^{high}$ PDX mice receiving RK-33 and IR, at day 27 one tumor broke through from the ablation to a terminal volume over the span of a week. This suggests a biological escape mechanism was initiated in at least one mouse receiving RK-33 radiosensitization. Future studies are warranted to investigate potential pro-survival pathways or cell populations (i.e., cancer stem cells, stromal cells in the microenvironment, etc.), which could contribute to tumor recurrence following radiosensitization of EWS via DDX3 impairment.

Although the complete array of mechanisms by which DDX3 enhances radiotherapy efficacy remains largely unknown, our findings suggest that modulation of the subcellular localization of RAD51 is a key part of this process. Impairment of DDX3 by RK-33 has previously been shown to radiosensitize prostate,[74] medulloblastoma[78] and lung cancer,[12] but the mechanisms behind these observations have not been elucidated. One study found that RK-33 radiosensitization in breast cancer involves abrogation of mitochondrial translation with concurrent increases in reactive oxygen species.[24] In the context of human hepatocellular carcinoma, *in vivo* genomic loss of DDX3X in liver tissue resulted in increased single-strand break and DSB signaling, as well as decreased expression of nucleotide excision repair proteins that resulted in liver tumorigenesis.[79] These studies indicate an important role for DDX3 in maintaining genomic stability through mechanisms of DDR. Recent studies have also implicated a role for DDX3 function in NHEJ repair of DSBs.[12] When we examined DDR pathways affected by DDX3 function, we found that both NHEJ and HR repair were impaired with siDDX3 knockdown. In contrast to previous studies where translation and protein expression were altered following DDX3 impairment, we detected no gross alterations in HR/NHEJ DDR protein abundance nor double-strand break signaling following RK-33 treatment in EWS. Instead, co-immunoprecipitation experiments revealed protein-protein interactions between DDX3 and select HR proteins but not proteins involved in NHEJ. Although both immunofluorescent and subcellular fractionation studies identified DDX3 in both the nuclear and cytoplasmic compartments of EWS, endogenous DDX3 did not co-localize with DSBs in the nucleus, suggesting that DDX3 does not robustly interact with DDR proteins at the site of DNA repair and is thus unlikely to contribute to DDR at sites of DSBs.

In conclusion, we report a novel mechanism of radiosensitization whereby DDR is impaired due to cytoplasmic sequestration of RAD51 following the inhibition of DDX3 RNA helicase activity. Cytoplasmic sequestration of RAD51 was dependent on the presence of cytoplasmic RNA:DNA hybrid structures. Importantly, we found that DDX3 helicase activity plays an active role in modulating cytoplasmic RNA:DNA hybrid levels, thus indirectly regulating RAD51 subcellular localization, and thereby inducing radiosensitization of EWS. These data further emphasize the importance of DDR protein localization in cancer biology and the need to develop new therapeutics directed at manipulating DDR protein localization. Additional studies are needed to determine whether a cytoplasmic DDX3-RNA:DNA hybrid-RAD51 complex is also present in other solid tumors that can potentially be targeted with radiation therapy and RK-33 treatment. Indeed, therapies aimed at leveraging the biological effects of genomic instability hold promise for increasing the potency and efficacy of clinical radiation therapy in multiple cancer types.

Limitations of the study

Ewing sarcoma is a low mutagenic neoplasia where the main oncogenic driver is caused by a chromosomal translocation and resultant fusion protein. Although genomic instability is present in many cancers, it remains to be determined whether a cytoplasmic DDX3-RNA:DNA hybrid-RAD51 complex is present or biologically relevant in tumors with alternate chromosomal translocations or high levels of mutagenicity. DDX3 is a multifaceted enzyme that contributes to many cellular pathways implicated in RNA biology, translation, the innate immune system, and oncogenesis. Therefore, additional roles for DDX3 in EWS biology could also contribute to the radiosensitizing effects of DDX3 inhibition in EWS as RPA32, RECQL1, and XRCC2, all of which are involved with HR, also physically associated with DDX3 in our immunoprecipitation experiments.

STAR★METHODS

Detailed methods are provided in the online version of this paper and include the following:

- KEY RESOURCES TABLE
- RESOURCE AVAILABILITY
  - Lead contact
  - Materials availability
  - Data and code availability
- EXPERIMENTAL MODELS AND STUDY PARTICIPANT DETAILS
  - Mouse models and studies
  - Xenograft models
  - Primary Cell Cultures
- METHOD DETAILS
  - Radiosensitization assay
  - Clonogenic assays
  - Immunofluorescence
  - Tissue microarray immunohistochemistry
  - DNA damage repair assays
  - Western blotting
  - Immunoprecipitations
  - Subcellular fractionations
  - Lentiviral Isolation and Transduction of RNaseH1 WT and RNaseH1 D210N
- QUANTIFICATION AND STATISTICAL ANALYSIS

SUPPLEMENTAL INFORMATION

Supplemental information can be found online at https://doi.org/10.1016/j.isci.2024.108925.

ACKNOWLEDGMENTS

We thank N, Ghazale, J.Biswas, R.Singer, and T. Bowman for the generous donation of the ubc-Hu-RNASEH1-3xHA and ubc-Hu-RNASEH1-D210N-Halo-3xHA lentiviral vectors; T. Bowman and A. Baker for helpful insights and discussions; and H. Guzik and V. DesMarais of AECOM Analytical Imaging Facility for training and technical assistance, supported by NCI cancer center support grant P30CA013330. This work was funded in part by Alex's Lemonade Stand Foundation and by the Montefiore Einstein Cancer Center Support Grant Number 2P30CA013330. V.R. was supported by a grant from FAMRI. A.J.R.B. was supported by the National Institutes of Health R01CA152063 and 1R01CA241554, the Cancer Prevention and Research Institute of Texas RP150445, and the Stand Up 2 Cancer-Cancer Research UK RT6187. A.G. was supported by American Association for Cancer Research-AstraZeneca Stimulating Therapeutic Advances through Research Training grant 18-4012-GORT. ABTR14B2-Q was supported by NCTN Operations Center Grant U10 CA180886, Human Specimen Banking Grant U24 CA114766, and NCTN Statistics & Data Center Grant U10 CA 180899 of the Children's Oncology Group from the National Cancer Institute of the National Institutes of Health. Additional support for research was provided by a grant from the WWWW (QuadW) Foundation, Inc. (www.QuadW.org) to the Children's Oncology Group. Disclaimer: the content is solely the responsibility of the authors and does not necessarily represent the official views of the National Institutes of Health.

AUTHOR CONTRIBUTIONS

Conceptualization, M.E.R., M.A., B.A.W., V.R., A.J.R.B., and D.M.L.; methodology, M.E.R., M.A., A.G., B.A.W., V.R., A.J.R.B., and D.M.L.; validation, M.E.R., M.A., A.G., R.W., B.A.W., J.W., and N.tH.; formal analysis, M.E.R., M.A., A.G., and B.A.W.; investigation, M.E.R., M.A., A.G., R.W., B.A.W., J.W., P.C., and N.tH.; resources, P.J.vD., V.R., A.J.R.B., and D.M.L.; writing—original draft, M.E.R., M.A., A.G., and D.M.L.; writing—review & editing, M.E.R., M.A., A.G., B.A.W., P.J.vD., V.R., A.J.R.B., and D.M.L; visualization, M.E.R., M.A., A.G., and R.W.; supervision, P.J.vD., A.J.R.B., and D.M.L.; funding acquisition, A.G., P.J.vD., V.R., A.J.R.B., and D.M.L.

DECLARATION OF INTERESTS

The authors declare no competing interests.

Received: May 30, 2023
Revised: December 9, 2023
Accepted: January 12, 2024
Published: January 16, 2024

REFERENCES

1. Riggi, N., Suvà, M.L., and Stamenkovic, I. (2021). Ewing's Sarcoma. N. Engl. J. Med. *384*, 154–164.
2. Bernstein, M.L., Devidas, M., Lafreniere, D., Souid, A.K., Meyers, P.A., Gebhardt, M., Stine, K., Nicholas, R., Perlman, E.J., Dubowy, R., et al. (2006). Intensive therapy with growth factor support for patients with Ewing tumor metastatic at diagnosis: Pediatric Oncology Group/Children's Cancer Group Phase II Study 9457–a report from the Children's Oncology Group. J. Clin. Oncol. *24*, 152–159.
3. Brohl, A.S., Solomon, D.A., Chang, W., Wang, J., Song, Y., Sindiri, S., Patidar, R., Hurd, L., Chen, L., Shern, J.F., et al. (2014). The genomic landscape of the Ewing Sarcoma family of tumors reveals recurrent STAG2 mutation. PLoS Genet. *10*, e1004475.
4. Crompton, B.D., Stewart, C., Taylor-Weiner, A., Alexe, G., Kurek, K.C., Calicchio, M.L., Kiezun, A., Carter, S.L., Shukla, S.A., Mehta, S.S., et al. (2014). The genomic landscape of pediatric Ewing sarcoma. Cancer Discov. *4*, 1326–1341.
5. Putnam, A.A., and Jankowsky, E. (2013). DEAD-box helicases as integrators of RNA, nucleotide and protein binding. Biochim. Biophys. Acta *1829*, 884–893.
6. Bourgeois, C.F., Mortreux, F., and Auboeuf, D. (2016). The multiple functions of RNA helicases as drivers and regulators of gene expression. Nat. Rev. Mol. Cell Biol. *17*, 426–438.
7. Abdelhaleem, M. (2004). Over-expression of RNA helicases in cancer. Anticancer Res. *24*, 3951–3953.
8. Bol, G.M., Xie, M., and Raman, V. (2015). DDX3, a potential target for cancer treatment. Mol. Cancer *14*, 188.
9. Erkizan, H.V., Uversky, V.N., and Toretsky, J.A. (2010). Oncogenic partnerships: EWS-FLI1 protein interactions initiate key pathways of Ewing's sarcoma. Clin. Cancer Res. *16*, 4077–4083.
10. Wilky, B.A., Kim, C., McCarty, G., Montgomery, E.A., Kammers, K., DeVine, L.R., Cole, R.N., Raman, V., and Loeb, D.M. (2016). RNA helicase DDX3: a novel therapeutic target in Ewing sarcoma. Oncogene *35*, 2574–2583.
11. Kondaskar, A., Kondaskar, S., Kumar, R., Fishbein, J.C., Muvarak, N., Lapidus, R.G., Sadowska, M., Edelman, M.J., Bol, G.M., Vesuna, F., et al. (2010). Novel, Broad Spectrum Anti-Cancer Agents Containing the Tricyclic 5:7:5-Fused Diimidazodiazepine Ring System. ACS Med. Chem. Lett. *2*, 252–256.
12. Bol, G.M., Vesuna, F., Xie, M., Zeng, J., Aziz, K., Gandhi, N., Levine, A., Irving, A., Korz, D., Tantravedi, S., et al. (2015). Targeting DDX3 with a small molecule inhibitor for lung cancer therapy. EMBO Mol. Med. *7*, 648–669.
13. Bol, G.M., Khan, R., Heerma van Voss, M.R., Tantravedi, S., Korz, D., Kato, Y., and Raman, V. (2015). PLGA nanoparticle formulation of RK-33: an RNA helicase inhibitor against DDX3. Cancer Chemother. Pharmacol. *76*, 821–827.
14. Brown, L.C., Lester, R.A., Grams, M.P., Haddock, M.G., Olivier, K.R., Arndt, C.A.S., Rose, P.S., and Laack, N.N. (2014). Stereotactic body radiotherapy for metastatic and recurrent ewing sarcoma and osteosarcoma. Sarcoma *2014*, 418270.
15. Andreou, D., Ranft, A., Gosheger, G., Timmermann, B., Ladenstein, R., Hartmann, W., Bauer, S., Baumhoer, D., van den Berg, H., Dijkstra, P.D.S., et al. (2020). Which Factors Are Associated with Local Control and Survival of Patients with Localized Pelvic Ewing's Sarcoma? A Retrospective Analysis of Data from the Euro-EWING99 Trial. Clin. Orthop. Relat. Res. *478*, 290–302.
16. Volchenboum, S.L., Andrade, J., Huang, L., Barkauskas, D.A., Krailo, M., Womer, R.B., Ranft, A., Potratz, J., Dirksen, U., Triche, T.J., and Lawlor, E.R. (2015). Gene Expression Profiling of Ewing Sarcoma Tumors Reveals the Prognostic Importance of Tumor-Stromal Interactions: A Report from the Children's Oncology Group. J. Pathol. Clin. Res. *1*, 83–94.
17. Rogakou, E.P., Pilch, D.R., Orr, A.H., Ivanova, V.S., and Bonner, W.M. (1998). DNA double-stranded breaks induce histone H2AX phosphorylation on serine 139. J. Biol. Chem. *273*, 5858–5868.
18. Gorthi, A., Romero, J.C., Loranc, E., Cao, L., Lawrence, L.A., Goodale, E., Iniguez, A.B., Bernard, X., Masamsetti, V.P., Roston, S., et al. (2018). EWS-FLI1 increases transcription to cause R-loops and block BRCA1 repair in Ewing sarcoma. Nature *555*, 387–391.
19. Bennardo, N., Cheng, A., Huang, N., and Stark, J.M. (2008). Alternative-NHEJ is a mechanistically distinct pathway of mammalian chromosome break repair. PLoS Genet. *4*, e1000110.
20. Stark, J.M., Pierce, A.J., Oh, J., Pastink, A., and Jasin, M. (2004). Genetic steps of mammalian homologous repair with distinct mutagenic consequences. Mol. Cell Biol. *24*, 9305–9316.
21. Guha, S., and Bhaumik, S.R. (2022). Transcription-coupled DNA double-strand break repair. DNA Repair *109*, 103211.
22. Sharma, D., Putnam, A.A., and Jankowsky, E. (2017). Biochemical Differences and Similarities between the DEAD-Box Helicase Orthologs DDX3X and Ded1p. J. Mol. Biol. *429*, 3730–3742.
23. He, Y., Zhang, D., Yang, Y., Wang, X., Zhao, X., Zhang, P., Zhu, H., Xu, N., and Liang, S. (2018). A double-edged function of DDX3, as an oncogene or tumor suppressor, in cancer progression (Review). Oncol. Rep. *39*, 883–892.
24. Heerma van Voss, M.R., Vesuna, F., Bol, G.M., Afzal, J., Tantravedi, S., Bergman, Y., Kammers, K., Lehar, M., Malek, R., Ballew, M., et al. (2018). Targeting mitochondrial translation by inhibiting DDX3: a novel radiosensitization strategy for cancer treatment. Oncogene *37*, 63–74.
25. Cortez, D., Wang, Y., Qin, J., and Elledge, S.J. (1999). Requirement of ATM-dependent phosphorylation of brca1 in the DNA damage response to double-strand breaks. Science *286*, 1162–1166.
26. Gatei, M., Scott, S.P., Filippovitch, I., Soronika, N., Lavin, M.F., Weber, B., and Khanna, K.K. (2000). Role for ATM in DNA damage-induced phosphorylation of BRCA1. Cancer Res. *60*, 3299–3304.
27. Ashley, A.K., Shrivastav, M., Nie, J., Amerin, C., Troksa, K., Glanzer, J.G., Liu, S., Opiyo, S.O., Dimitrova, D.D., Le, P., et al. (2014). DNA-PK phosphorylation of RPA32 Ser4/Ser8 regulates replication stress checkpoint activation, fork restart, homologous recombination and mitotic catastrophe. DNA Repair *21*, 131–139.
28. Taricani, L., Shanahan, F., and Parry, D. (2009). Replication stress activates DNA polymerase alpha-associated Chk1. Cell Cycle *8*, 482–489.
29. Meek, K., Gupta, S., Ramsden, D.A., and Lees-Miller, S.P. (2004). The DNA-dependent protein kinase: the director at the end. Immunol. Rev. *200*, 132–141.
30. Croteau, D.L., Popuri, V., Opresko, P.L., and Bohr, V.A. (2014). Human RecQ helicases in DNA repair, recombination, and replication. Annu. Rev. Biochem. *83*, 519–552.
31. Sullivan, M.R., and Bernstein, K.A. (2018). RAD-ical New Insights into RAD51 Regulation. Genes *9*, 629.
32. Plo, I., Laulier, C., Gauthier, L., Lebrun, F., Calvo, F., and Lopez, B.S. (2008). AKT1 inhibits homologous recombination by inducing cytoplasmic retention of BRCA1 and RAD51. Cancer Res. *68*, 9404–9412.
33. Jefford, C.E., Feki, A., Harb, J., Krause, K.H., and Irminger-Finger, I. (2004). Nuclear-cytoplasmic translocation of BARD1 is linked to its apoptotic activity. Oncogene *23*, 3509–3520.
34. Francis, D.B., Kozlov, M., Chavez, J., Chu, J., Malu, S., Hanna, M., and Cortes, P. (2014). DNA Ligase IV regulates XRCC4 nuclear localization. DNA Repair *21*, 36–42.
35. Moudry, P., Lukas, C., Macurek, L., Neumann, B., Heriche, J.K., Pepperkok, R., Ellenberg, J., Hodny, Z., Lukas, J., and Bartek, J. (2012). Nucleoporin NUP153 guards genome integrity by promoting nuclear import of 53BP1. Cell Death Differ. *19*, 798–807.
36. Low, L.H., Chow, Y.L., Li, Y., Goh, C.P., Putz, U., Silke, J., Ouchi, T., Howitt, J., and Tan, S.S. (2015). Nedd4 family interacting protein 1 (Ndfip1) is required for ubiquitination and nuclear trafficking of BRCA1-associated ATM

activator 1 (BRAT1) during the DNA damage response. J. Biol. Chem. *290*, 7141–7150.
37. Chappidi, N., De Gregorio, G., and Ferrari, S. (2019). Replication stress-induced Exo1 phosphorylation is mediated by Rad53/Pph3 and Exo1 nuclear localization is controlled by 14-3-3 proteins. Cell Div. *14*, 1.
38. Ohali, A., Avigad, S., Cohen, I.J., Meller, I., Kollender, Y., Issakov, J., Goshen, Y., Yaniv, I., and Zaizov, R. (2004). High frequency of genomic instability in Ewing family of tumors. Cancer Genet. Cytogenet. *150*, 50–56.
39. Embree, L.J., Azuma, M., and Hickstein, D.D. (2009). Ewing sarcoma fusion protein EWSR1/FLI1 interacts with EWSR1 leading to mitotic defects in zebrafish embryos and human cell lines. Cancer Res. *69*, 4363–4371.
40. Ragu, S., Matos-Rodrigues, G., and Lopez, B.S. (2020). Replication Stress, DNA Damage, Inflammatory Cytokines and Innate Immune Response. Genes *11*, 409.
41. Wang, I.X., Grunseich, C., Fox, J., Burdick, J., Zhu, Z., Ravazian, N., Hafner, M., and Cheung, V.G. (2018). Human proteins that interact with RNA/DNA hybrids. Genome Res. *28*, 1405–1414.
42. Paulsen, R.D., Soni, D.V., Wollman, R., Hahn, A.T., Yee, M.C., Guan, A., Hesley, J.A., Miller, S.C., Cromwell, E.F., Solow-Cordero, D.E., et al. (2009). A genome-wide siRNA screen reveals diverse cellular processes and pathways that mediate genome stability. Mol. Cell *35*, 228–239.
43. Stirling, P.C., Chan, Y.A., Minaker, S.W., Aristizabal, M.J., Barrett, I., Sipahimalani, P., Kobor, M.S., and Hieter, P. (2012). R-loop-mediated genome instability in mRNA cleavage and polyadenylation mutants. Genes Dev. *26*, 163–175.
44. Cerritelli, S.M., and Crouch, R.J. (2009). Ribonuclease H: the enzymes in eukaryotes. FEBS J. *276*, 1494–1505.
45. Boguslawski, S.J., Smith, D.E., Michalak, M.A., Mickelson, K.E., Yehle, C.O., Patterson, W.L., and Carrico, R.J. (1986). Characterization of monoclonal antibody to DNA.RNA and its application to immunodetection of hybrids. J. Immunol. Methods *89*, 123–130.
46. Chen, L., Chen, J.Y., Zhang, X., Gu, Y., Xiao, R., Shao, C., Tang, P., Qian, H., Luo, D., Li, H., et al. (2017). R-ChIP Using Inactive RNase H Reveals Dynamic Coupling of R-loops with Transcriptional Pausing at Gene Promoters. Mol. Cell *68*, 745–757.e5.
47. Schönborn, J., Oberstrass, J., Breyel, E., Tittgen, J., Schumacher, J., and Lukacs, N. (1991). Monoclonal antibodies to double-stranded RNA as probes of RNA structure in crude nucleic acid extracts. Nucleic Acids Res. *19*, 2993–3000.
48. Gildemeister, O.S., Sage, J.M., and Knight, K.L. (2009). Cellular redistribution of Rad51 in response to DNA damage: novel role for Rad51C. J. Biol. Chem. *284*, 31945–31952.
49. Browning, C.L., Wise, J.P., and Sr, , .. (2017). Prolonged exposure to particulate chromate inhibits RAD51 nuclear import mediator proteins. Toxicol. Appl. Pharmacol. *331*, 101–107.
50. Trojanek, J., Ho, T., Del Valle, L., Nowicki, M., Wang, J.Y., Lassak, A., Peruzzi, F., Khalili, K., Skorski, T., and Reiss, K. (2003). Role of the insulin-like growth factor I/insulin receptor substrate 1 axis in Rad51 trafficking and DNA repair by homologous recombination. Mol. Cell Biol. *23*, 7510–7524.
51. Alshareeda, A.T., Negm, O.H., Aleskandarany, M.A., Green, A.R., Nolan, C., TigHhe, P.J., Madhusudan, S., Ellis, I.O., and Rakha, E.A. (2016). Clinical and biological significance of RAD51 expression in breast cancer: a key DNA damage response protein. Breast Cancer Res. Treat. *159*, 41–53.
52. Bhattacharya, S., Srinivasan, K., Abdisalaam, S., Su, F., Raj, P., Dozmorov, I., Mishra, R., Wakeland, E.K., Ghose, S., Mukherjee, S., and Asaithamby, A. (2017). RAD51 interconnects between DNA replication, DNA repair and immunity. Nucleic Acids Res. *45*, 4590–4605.
53. Coquel, F., Silva, M.J., Técher, H., Zadorozhny, K., Sharma, S., Nieminuszczy, J., Mettling, C., Dardillac, E., Barthe, A., Schmitz, A.L., et al. (2018). SAMHD1 acts at stalled replication forks to prevent interferon induction. Nature *557*, 57–61.
54. Keskin, H., Shen, Y., Huang, F., Patel, M., Yang, T., Ashley, K., Mazin, A.V., and Storici, F. (2014). Transcript-RNA-templated DNA recombination and repair. Nature *515*, 436–439.
55. Lu, W.T., Hawley, B.R., Skalka, G.L., Baldock, R.A., Smith, E.M., Bader, A.S., Malewicz, M., Watts, F.Z., Wilczynska, A., and Bushell, M. (2018). Drosha drives the formation of DNA:RNA hybrids around DNA break sites to facilitate DNA repair. Nat. Commun. *9*, 532.
56. Zhang, C., Chen, L., Peng, D., Jiang, A., He, Y., Zeng, Y., Xie, C., Zhou, H., Luo, X., Liu, H., et al. (2020). METTL3 and N6-Methyladenosine Promote Homologous Recombination-Mediated Repair of DSBs by Modulating DNA-RNA Hybrid Accumulation. Mol. Cell *79*, 425–442.e7.
57. D'Alessandro, G., Whelan, D.R., Howard, S.M., Vitelli, V., Renaudin, X., Adamowicz, M., Iannelli, F., Jones-Weinert, C.W., Lee, M., Matti, V., et al. (2018). BRCA2 controls DNA:RNA hybrid level at DSBs by mediating RNase H2 recruitment. Nat. Commun. *9*, 5376.
58. Chen, M., Linstra, R., and van Vugt, M.A.T.M. (2022). Genomic instability, inflammatory signaling and response to cancer immunotherapy. Biochim. Biophys. Acta Rev. Canc *1877*, 188661.
59. Crossley, M.P., Song, C., Bocek, M.J., Choi, J.H., Kousorous, J., Sathirachinda, A., Lin, C., Brickner, J.R., Bai, G., Lans, H., et al. (2023). R-loop-derived cytoplasmic RNA-DNA hybrids activate an immune response. Nature *613*, 187–194.
60. Gu, L., Fullam, A., McCormack, N., Höhn, Y., and Schröder, M. (2017). DDX3 directly regulates TRAF3 ubiquitination and acts as a scaffold to co-ordinate assembly of signalling complexes downstream from MAVS. Biochem. J. *474*, 571–587.
61. Gu, L., Fullam, A., Brennan, R., and Schröder, M. (2013). Human DEAD box helicase 3 couples IkappaB kinase epsilon to interferon regulatory factor 3 activation. Mol. Cell Biol. *33*, 2004–2015.
62. Schröder, M., Baran, M., and Bowie, A.G. (2008). Viral targeting of DEAD box protein 3 reveals its role in TBK1/IKKepsilon-mediated IRF activation. EMBO J. *27*, 2147–2157.
63. Oshiumi, H., Sakai, K., Matsumoto, M., and Seya, T. (2010). DEAD/H BOX 3 (DDX3) helicase binds the RIG-I adaptor IPS-1 to up-regulate IFN-beta-inducing potential. Eur. J. Immunol. *40*, 940–948.
64. Wang, X., Wang, R., Luo, M., Li, C., Wang, H.X., Huan, C.C., Qu, Y.R., Liao, Y., and Mao, X. (2017). (DEAD)-box RNA helicase 3 modulates NF-kappaB signal pathway by controlling the phosphorylation of PP2A-C subunit. Oncotarget *8*, 33197–33213.
65. Fullam, A., Gu, L., Höhn, Y., and Schröder, M. (2018). DDX3 directly facilitates IKKalpha activation and regulates downstream signalling pathways. Biochem. J. *475*, 3595–3607.
66. Choi, H., Kwon, J., Cho, M.S., Sun, Y., Zheng, X., Wang, J., Bouker, K.B., Casey, J.L., Atkins, M.B., Toretsky, J., and Han, C. (2021). Targeting DDX3X Triggers Antitumor Immunity via a dsRNA-Mediated Tumor-Intrinsic Type I Interferon Response. Cancer Res. *81*, 3607–3620.
67. Mankan, A.K., Schmidt, T., Chauhan, D., Goldeck, M., Höning, K., Gaidt, M., Kubarenko, A.V., Andreeva, L., Hopfner, K.P., and Hornung, V. (2014). Cytosolic RNA:DNA hybrids activate the cGAS-STING axis. EMBO J. *33*, 2937–2946.
68. Rigby, R.E., Webb, L.M., Mackenzie, K.J., Li, Y., Leitch, A., Reijns, M.A.M., Lundie, R.J., Revuelta, A., Davidson, D.J., Diebold, S., et al. (2014). RNA:DNA hybrids are a novel molecular pattern sensed by TLR9. EMBO J. *33*, 542–558.
69. Yang, E.S., Nowsheen, S., Rahman, M.A., Cook, R.S., and Xia, F. (2012). Targeting BRCA1 localization to augment breast tumor sensitivity to poly(ADP-Ribose) polymerase inhibition. Cancer Res. *72*, 5547–5555.
70. Nowsheen, S., Cooper, T., Stanley, J.A., and Yang, E.S. (2012). Synthetic lethal interactions between EGFR and PARP inhibition in human triple negative breast cancer cells. PLoS One *7*, e46614.
71. Stringer-Reasor, E.M., May, J.E., Olariu, E., Caterinicchia, V., Li, Y., Chen, D., Della Manna, D.L., Rocque, G.B., Vaklavas, C., Falkson, C.I., et al. (2021). An open-label, pilot study of veliparib and lapatinib in patients with metastatic, triple-negative breast cancer. Breast Cancer Res. *23*, 30.
72. Qin, Q., Xie, H., Wise, S.S., Browning, C.L., Thompson, K.N., Holmes, A.L., Wise, J.P., and Sr, , .. (2014). Homologous recombination repair signaling in chemical carcinogenesis: prolonged particulate hexavalent chromium exposure suppresses the Rad51 response in human lung cells. Toxicol. Sci. *142*, 117–125.
73. Planas-Paz, L., Pliego-Mendieta, A., Hagedorn, C., Aguilera-Garcia, D., Haberecker, M., Arnold, F., Herzog, M., Bankel, L., Guggenberger, R., Steiner, S., et al. (2023). Unravelling homologous recombination repair deficiency and therapeutic opportunities in soft tissue and bone sarcoma. EMBO Mol. Med. *15*, e16863.
74. Xie, M., Vesuna, F., Tantravedi, S., Bol, G.M., Heerma van Voss, M.R., Nugent, K., Malek, R., Gabrielson, K., van Diest, P.J., Tran, P.T., and Raman, V. (2016). RK-33 Radiosensitizes Prostate Cancer Cells by Blocking the RNA Helicase DDX3. Cancer Res. *76*, 6340–6350.
75. Chen, C.C., Yang, J.H., Fu, S.L., Lin, W.J., and Lin, C.H. (2021). Arginine Methylation of hnRNPK Inhibits the DDX3-hnRNPK Interaction to Play an Anti-Apoptosis Role in Osteosarcoma Cells. Int. J. Mol. Sci. *22*, 9764.
76. Wang, L., Lawrence, M.S., Wan, Y., Stojanov, P., Sougnez, C., Stevenson, K., Werner, L., Sivachenko, A., DeLuca, D.S., Zhang, L., et al. (2011). SF3B1 and other novel cancer genes in

chronic lymphocytic leukemia. N. Engl. J. Med. *365*, 2497–2506.

77. Robinson, G., Parker, M., Kranenburg, T.A., Lu, C., Chen, X., Ding, L., Phoenix, T.N., Hedlund, E., Wei, L., Zhu, X., et al. (2012). Novel mutations target distinct subgroups of medulloblastoma. Nature *488*, 43–48.
78. Tantravedi, S., Vesuna, F., Winnard, P.T., Jr., Martin, A., Lim, M., Eberhart, C.G., Berlinicke, C., Raabe, E., van Diest, P.J., and Raman, V. (2019). Targeting DDX3 in Medulloblastoma Using the Small Molecule Inhibitor RK-33. Transl. Oncol. *12*, 96–105.
79. Chan, C.H., Chen, C.M., Lee, Y.H.W., and You, L.R. (2019). DNA Damage, Liver Injury, and Tumorigenesis: Consequences of DDX3X Loss. Mol. Cancer Res. *17*, 555–566.
80. Franken, N.A.P., Rodermond, H.M., Stap, J., Haveman, J., and van Bree, C. (2006). Clonogenic assay of cells in vitro. Nat. Protoc. *1*, 2315–2319.
81. Angus, A.G.N., Dalrymple, D., Boulant, S., McGivern, D.R., Clayton, R.F., Scott, M.J., Adair, R., Graham, S., Owsianka, A.M., Targett-Adams, P., et al. (2010). Requirement of cellular DDX3 for hepatitis C virus replication is unrelated to its interaction with the viral core protein. J. Gen. Virol. *91*, 122–132.

STAR★METHODS

KEY RESOURCES TABLE

REAGENT or RESOURCE	SOURCE	IDENTIFIER
Antibodies		
Rabbit monoclonal IgG anti-ATM (clone D2E2)	Cell Signaling Technology	Cat#2873; RRID: AB_2062659
Rabbit polyclonal IgG anti-ATR	Cell Signaling Technology	Cat#2790; RRID: AB_2227860
Rabbit monoclonal IgG anti-β-actin	Cell Signaling Technology	Cat#4970; RRID: AB_2223172
Mouse monoclonal IgG2b anti-β-2-microglobulin	Santa Cruz Biotechnology	Cat#sc-13565; RRID: AB_626748
Rabbit monoclonal IgG anti-β-2-microglobulin	Cell Signaling Technology	Cat#12851; RRID: AB_2716551
Rabbit polyclonal IgG anti-BRCA1	Cell Signaling Technology	Cat#9010; RRID: AB_2228244
Rabbit polyclonal IgG anti-Caspase 3	Abcam	Cat#ab13847; RRID: AB_443014
Mouse monoclonal IgG2a anti-Chk1	Santa Cruz Biotechnology	Cat#sc-8408; RRID: AB_627257
Rabbit polyclonal IgG anti-Chk1	Abcam	Cat#ab47574; RRID: AB_869133
Mouse monoclonal IgG2b anti-DDX3 (clone C-4)	Santa Cruz Biotechnology	Cat#sc-365768; RRID: AB_10844621
Rabbit polyclonal IgG anti-DDX3	Abcam	Cat#ab235940; RRID: AB_2910140
Mouse monoclonal IgG1 anti-eIF4E (clone P-2)	Santa Cruz Biotechnology	Cat#sc-9976; RRID: AB_627502
Rabbit polyclonal IgG anti-Histone H2A.X	Cell Signaling Technology	Cat#2595; RRID: AB_10694556
Mouse monoclonal IgG1 anti-HA	Sigma-Aldrich	Cat#H9658; RRID: AB_260092
Mouse monoclonal IgG2b anti-dsRNA (J2)	Cell Signaling Technology	Cat#76651L; RRID: AB_2936194
Mouse monoclonal IgG2b anti-Ku-70 (3F246)	Santa Cruz Biotechnology	Cat#sc-71469; RRID: AB_1125206
Mouse monoclonal IgG1 anti-Ku-86 (B-1)	Santa Cruz Biotechnology	Cat#sc-5280; RRID: AB_672929
Mouse monoclonal IgG1 anti-Mre11 (12D7)	Abcam	Cat#ab214; RRID: AB_302859
Rabbit polyclonal IgG anti-NUP205	Thermo Fisher Scientific	Cat#PA5-55112; RRID: AB_2644895
Rabbit polyclonal IgG anti-ATR, phospho (Ser428)	Cell Signaling Technology	Cat#2853; RRID: AB_2290281
Rabbit polyclonal IgG anti-BRCA1, phospho (Ser1432)	Abcam	Cat#ab194753; RRID: AB_2910141
Rabbit monoclonal IgG anti-Chk1, phospho (Ser345) (clone 133D3)	Cell Signaling Technology	Cat#2348; RRID: AB_331212
Mouse monoclonal IgG1 anti-Histone H2A.X, phospho (Ser139) (clone JBW301)	Millipore Sigma	Cat#05-636; RRID: AB_309864
Rabbit monoclonal IgG anti-Histone H2A.X, phospho (Ser139) (clone 20E3)	Cell Signaling Technology	Cat#9718; RRID: AB_2118009
Rabbit polyclonal IgG anti-RPA32 (Ser4/Ser8)	Bethyl Laboratories	Cat#A300-245A; RRID: AB_210547
Mouse monoclonal IgG1 anti-Rad50 (clone 13B3/2C6)	Abcam	Cat#ab89; RRID: AB_2176935
Mouse monoclonal IgG1 anti-Rad51 (clone G-9)	Santa Cruz Biotechnology	Cat#sc-377467; RRID: AB_2910142
Rabbit polyclonal IgG anti-Rad51	Abcam	Cat#ab63801; RRID: AB_1142428
Rabbit monoclonal IgG anti-Rad52 [clone EPR3464(2)]	Abcam	Cat#ab124971; RRID: AB_10971685
Mouse monoclonal IgG2a anti-RecQL1 (clone A-9)	Santa Cruz Biotechnology	Cat#sc-166388; RRID: AB_2178425
Mouse monoclonal IgG1 anti-RPA32/RPA2 (clone 9H8)	Abcam	Cat#ab2175; RRID: AB_302873

(*Continued on next page*)

Continued

REAGENT or RESOURCE	SOURCE	IDENTIFIER
Rabbit monoclonal IgG anti-RPA32/RPA2 (clone EPR2877Y)	Abcam	Cat#ab76420; RRID: AB_1524336
Mouse monoclonal IgG2a anti-RNA:DNA hybrids (clone S9.6)	Boguslawski et al., 1986[45]	N/A
Rabbit IgG anti-RNA:DNA hybrids (clone S9.6)	Kerafast	Cat# Kf-Ab01137-23.0; RRID: AB_2936195
Mouse monoclonal IgG3 anti-ssDNA (clone TNT-3)	EMD Millipore	Cat#MAB3868; RRID: AB_570342
Rabbit polyclonal IgG anti-XPG	Proteintech	Cat#11331-1-AP; RRID: AB_2098155
Mouse monoclonal IgG2a anti-XRCC2 (clone F-4)	Santa Cruz Biotechnology	Cat#sc-365854; RRID: AB_10846464
Mouse monoclonal IgG2a anti-XRCC4 (clone C-4)	Santa Cruz Biotechnology	Cat#sc-271087; RRID: AB_10612396
Mouse IgG1 Isotype Control (clone MOPC-21)	Thermo Fisher Scientific	Cat#MA1-10407; RRID: AB_2536775
Mouse IgG2a Isotype Control (clone eBM2a)	Thermo Fisher Scientific	Cat#14-4724-85; RRID: AB_470115
Mouse IgG2b Isotype Control	Thermo Fisher Scientific	Cat#02-6300; RRID: AB_2532949
Mouse IgG3 Isotype Control (clone B10)	Thermo Fisher Scientific	Cat#14-4742-82; RRID: AB_470120
Rabbit IgG Isotype Control (clone SP137)	Thermo Fisher Scientific	Cat#MA5-16384; RRID: AB_2537903
Horse anti-mouse IgG (H+L), HRP	Vector Laboratories	Cat#PI-2000; RRID: AB_2336177
Goat anti-mouse IgG1, Cross-Adsorbed, Alexa Fluor 488 Conjugated	Thermo Fisher Scientific	Cat#A-21121; RRID: AB_2535764
Goat anti-mouse IgG1, Cross-Adsorbed, Alexa Fluor 555 Conjugated	Thermo Fisher Scientific	Cat#A-21127; RRID: AB_2535769
Goat anti-mouse IgG2a, Cross-Adsorbed, Alexa Fluor 488 Conjugated	Thermo Fisher Scientific	Cat#A-21131; RRID: AB_2535771
Goat anti-mouse IgG2a, Cross-Adsorbed, Alexa Fluor 594 Conjugated	Thermo Fisher Scientific	Cat#A-21135; RRID: AB_2535774
Goat anti-mouse IgG2a, Cross-Adsorbed, Alexa Fluor 647 Conjugated	Thermo Fisher Scientific	Cat#A-21241; RRID: AB_2535810
Goat anti-mouse IgG2b, Cross-Adsorbed, Alexa Fluor 594 Conjugated	Thermo Fisher Scientific	Cat#A-21145; RRID: AB_2535781
Goat anti-mouse IgG2b, Cross-Adsorbed, Alexa Fluor 647 Conjugated	Thermo Fisher Scientific	Cat#A-21242; RRID: AB_2535811
Goat anti-mouse IgG3, Cross-Adsorbed, Alexa Fluor 488 Conjugated	Thermo Fisher Scientific	Cat#A-21151; RRID: AB_2535784
Goat anti-rabbit IgG (H+L), Cross-Adsorbed, Alexa Fluor 555 Conjugated	Thermo Fisher Scientific	Cat#A-21428; RRID: AB_2535849
Goat anti-rabbit IgG (H+L), HRP	Vector Laboratories	Cat#PI-1000; RRID: AB_2336198
Biological samples		
Human Ewing sarcoma tumor microarray	Children's Oncology Group	Project# ABTR14B2-Q
EWS-1	Laboratory of Chand Khanna	N/A
EWS-4	Laboratory of Chand Khanna	N/A
EWS-6	Laboratory of Chand Khanna	N/A
JHH-ESX-1	This paper	N/A
JHH-ESX-2	This paper	N/A
JHH-ESX-3	This paper	N/A
Human Ewing sarcoma biopsy samples	Montefiore Medical Center, Department of Pathology	N/A

(*Continued on next page*)

Continued

REAGENT or RESOURCE	SOURCE	IDENTIFIER
Chemicals, peptides, and recombinant proteins		
Crystal Violet, pure, indicator	Thermo Scientific Chemicals	Cat#212120250
FuGENE® HD Transfection Reagent	Promega	Cat# E2311
RK-33	Laboratory of Venu Raman	CAS# 1070773-09-9
Surebeads™ Protein G Magnetic Beads	Bio-Rad Laboratories	Cat# 1614023
Surebeads™ Protein A Magnetic Beads	Bio-Rad Laboratories	Cat# 1614013
Critical commercial assays		
ATTC Universal Mycoplasma Detection Kit	Fischer Scientific	Cat#ATCC301012K
DC™ Protein Assay Kit II	Bio-Rad Laboratories	Cat#5000112
NE PER Nuclear and Cytoplasmic Extraction Kit	Thermo Scientific	Cat# PI78833
Novolink Polymer Detection System	Leica Microsystems	Cat#RE7280-CE
Experimental models: Cell lines		
A4573	Laboratory of Katia Scotlandi	RRID:CVCL_6245
HEK293T	ATCC	CRL-157; RRID:CVCL_0063
MHH-ES-1	DSMZ-German Collection of Microorganisms and Cell Cultures	ACC-167; RRID:CVCL_1411
TC32	Children's Cancer Respository	https://cccells.org; RRID:CVCL_7151
TC71	Children's Cancer Repository	https://cccells.org; RRID:CVCL_2213
U2OS DR-GFP	Laboratory of Jeremy Stark	RRID:CVCL_B0A7
U2OS EJ5-GFP	Laboratory of Jeremy Stark	N/A
U2OS SSA-GFP	Laboratory of Jeremy Stark	N/A
Experimental models: Organisms/strains		
NOD.Cg-*Prkdc*^{scid} *Il2rg*^{tm1Wjl}/SzJ (NSG) mice	The Jackson Laboratory	Strain #:005557; RRID: IMSR_JAX:005557
Recombinant DNA		
ubc-Hu-rnaseH1-3xHA (RNaseH1 WT)	Laboratory of Robert Singer	N/A
ubc-Hu-RNASEH1-D210N-Halo-3xHA (RNaseH1 D210N)	Laboratory of Robert Singer	N/A
I*Sce*I-pCAGGS	Laboratory of Jeremy Stark	N/A
Software and algorithms		
ImageJ2, version 2.3.0/1.53f software	NIH	imagej.nih.gov/ij
Volocity® software	Quorum Technologies	www.perkinelmer.com
GraphPad Prism 9.3.1 software	GraphPad Software	www.graphpad.com
Adobe Photoshop 2021, version 22.4.3	Adobe	www.adobe.com

RESOURCE AVAILABILITY

Lead contact

Further information and requests concerning resources and reagents should be directed to and will be fulfilled by the lead contact, David M. Loeb, MD, PhD (david.loeb@einsteinmed.edu).

Materials availability

This study did not create any novel research reagents.

Data and code availability

Data: The data generated in this study are available upon request from the lead contact.

Code: This paper does not report original code.

Any additional information required to reanalyze the data reported in this paper is available from the lead contact upon request.

EXPERIMENTAL MODELS AND STUDY PARTICIPANT DETAILS

Mouse models and studies

All mice procedures were approved by the Johns Hopkins Animal Care and Use Committee. Female, 3- to 6-month-old NOD.Cg-*Prkdc*^{scid} *Il2rg*^{tm1Wjl}/SzJ (Strain #:005557; RRID:IMSR_JAX:005557) mice (JHU breeding colony, Baltimore, MD, USA) were used for experiments, with sample size of 10 randomly selected mice with equivalent numbers per cohort. Freshly isolated 3 mm^3 EWS-4 and JHHES-X3 xenograft fragments coated with Matrigel (BD Biosciences) were implanted in the subcutaneous flanks. Once palpable, 7–9 mm^3, animals bearing xenografts were randomly divided into 4 cohorts depending on treatments received: control (DMSO only), DMSO+IR, RK33 only, or RK33+IR). Either 50 mg/kg RK-33 or equivalent volume of 50 μl DMSO was injected intraperitoneal every other day for one week for a total of 3 treatments. After which, mice were exposed to 10 Gy IR 6 hours following the third injection using a small animal radiation research platform (SARPP) in the institutional Experimental Irradiators Core. Three more injections of DMSO or RK-33 every other day were administered in the following week post-IR. Tumor dimensions were measured twice weekly using calipers until reaching a diameter of ≥15 mm. Volumes were calculated using an elliptical formula and normalized to the initial tumor volume. No blinding was employed.

Xenograft models

EWS-4 PDX was a gift from Chand Khanna (National Cancer Institute, Bethesda, MD) while the JHH-ESX-1, JHH-ESX-2, and JHH-ESX-3 xenografts were generated in our laboratory on a tumor banking protocol approved by Johns Hopkins University School of Medicine IRB. EWS xenografts were coated with Matrigel basement membrane (BD Biosciences, Bedford, MA, USA) and implanted subcutaneously into NOD.Cg-*Prkdc*^{scid} *Il2rg*^{tm1Wjl}/SzJ (NSG, Strain #:005557; RRID:IMSR_JAX:005557) mice purchased from The Jackson Laboratory (Bar Harbor, ME, USA). All PDXs were passaged subcutaneously in NSG mice at least 3 times prior to experimental usage.

Primary Cell Cultures

Established EWS cell lines TC71 (RRID:CVCL_2213) and TC32 (RRID:CVCL_7151) were acquired from Children's Cancer Respository (https://cccells.org), A4573 (RRID:CVCL_6245) was a kind gift from the laboratory of Katia Scotlandi, and MHH-ES-1 (ACC-167; RRID:CVCL_1411) was purchased from German Collection of Microorganisms and Cell Cultures (dsmz.de, Braunschweig, Germany). Cell lines were validated using short-tandem repeat (STR) profiling at Albert Einstein College of Medicine's (AECOM) Department of Genetics Genomic Core. HEK293T cells (CRL-157; RRID:CVCL_0063) were purchased from American Type Culture Collection (ATCC, Manassas, VA, USA). U2OS cells containing an integrated copy of each reporter and the homing endonuclease I*Sce*I in pCAGGS vectors with control were kind gifts from Dr. Maria Jasin (Memorial Sloan Kettering Cancer Center, New York, USA) and Dr. Jeremy Stark (City of Hope, California, USA). DDX3 shRNA knockdown cell lines were generated as previously described by Wilky et al. (2016). Cell lines were cultured in RPMI 1640 medium (Gibco-ThermoFisher Scientific, Waltham, MA, USA) containing 10% heat-inactivated fetal bovine serum (Atlanta Biologicals, Flowery Branch, GA, USA) at 37°C in 5% CO_2. Cell lines were passaged between 6 to 10 times using 0.25% trypsin-EDTA (Gibco-ThermoFisher Scientific) between thawing and experimental collection. ATTC Universal Mycoplasma Detection Kit (ATCC 301012K, Fischer Scientific, Waltham, MA) was used per manufacturer's instructions to screen cultures every 3 to 6 months to confirm absence of mycoplasma infection.

METHOD DETAILS

Radiosensitization assay

EWS cells were either grown in 4 well chamber slides (Nunc Lab-Tek II Chamber Slide™ system, Thermo Scientific, Hudson, NH, USA) at a density of 140,000 cells/well or in 6 well plates at densities ranging from 2.5 to 5 x 10^5 cells on coverslips coated with bovine collagen type I (Gibco-Thermo Fisher Scientific) and incubated for 24 hours at 37°C and 5% CO_2. RK-33 (CAS# 1070773-09-9) was dissolved in dimethyl sulfoxide (DMSO, Sigma-Aldrich) and added to the cultured cells 45–60 minutes prior to IR (2 Gy). The cells were maintained at 37°C and 5% CO_2 until the desired timepoint.

Clonogenic assays

Clonogenic assays were performed as previously described.[80] Briefly, radiosensitization assays were performed using EWS cells as described above. Six hours following IR, cells were detached from the plate using 0.25% trypsin-EDTA (Gibco-ThermoFisher Scientific). Clonal densities of 400 or 800 cells/well in 6 well plates containing conditioned media were then plated in triplicate. Cells were then grown at 37°C and 5% CO_2 for 5 days undisturbed. Clones were then fixed with 4% paraformaldehyde (Thermo Scientific) at room temperature for 30 minutes and stained with 0.5% crystal violet in methanol. Clones were imaged using the ChemiDoc™ Touch Imaging System (RRID:SCR_021693, Bio-Rad Laboratories) and numbers of clones were quantified using ImageJ2, version 2.3.0/1.53f software (RRID:SCR_003070, NIH, Bethesda, MD). The analysis of clone numbers was performed blinded.

Immunofluorescence

For immunofluorescent staining, cells were fixed with 4% paraformaldehyde (Thermo Scientific) for 10 mins, washed 1x with phosphate buffered saline (PBS), permeabilized using 0.2% Triton-X in PBS for 15 mins, then blocked for 30 minutes using 5% goat serum, 1% bovine serum albumin (BSA), 0.2% Triton-X PBS blocking buffer. Slides were then incubated with primary antibodies (Table S1) diluted in blocking buffer overnight at 4°C. Slides were washed 3 times with 0.1% Tween™ 20 (Thermo Fisher Scientific) PBS the next day followed by 1 hour incubation at room temperature with fluorophore labeled secondary antibodies (Table S1) diluted in blocking buffer. Slides were then washed 3x with PBS and mounted the coverslips to slides using ProLong™ Diamond Antifade Mountant with diamidino-2-phenylindole (DAPI) (Thermo Fisher Scientific). Slides were imaged using AECOM's Analytical Imaging Facility's Leica SP5 Acousto-Optical Beam Splitter (Leica Microcystems, Wetzlar, Germany) confocal microscope. Adobe Photoshop 2021 (RRID:SCR_014199, Adobe, San Jose, CA, USA) was used to globally process images for contrast, size, and brightness. Images were quantified using either ImageJ2 software (RRID:SCR_003070, NIH) or Volocity® software (RRID:SCR_002668, Quorum Technologies, Puslinch, Ontario, Canada).

Tissue microarray immunohistochemistry

The EWS tissue microarrays were provided by the Children's Oncology Group through project ABTR14B2-Q. Following deparaffination in xylene and the samples were rehydrated in decreasing ethanol dilutions. Endogenous peroxidase activity was blocked by endogenous peroxidase from Novolink Polymer Detection System (Leica Microsystems, Eindhoven, The Netherlands) and was followed by antigen retrieval by boiling for 20 minutes in EDTA buffer (pH 9.0). Slides were blocked with protein block from Novolink Polymer Detection System and subsequently incubated in a humidified chamber for 1 hour with anti-DDX3 (1:50, mAb AO196, RRID:AB_2936197, Sigma Aldrich).[81] Post primary block, secondary antibodies and diaminobenzidine treatment were performed with the same Novolink Polymer Detection System according to the manufacturer's instructions. The slides were lightly counterstained with hematoxylin and mounted. Images were scored for staining intensity using a scale of 0 to +3 by Dr. Paul J. van Diest, University Medical Center Utrecht, The Netherlands. The slides were scanned using a Hamamatsu, NanoZoomer XR C12000-21/-22.

DNA damage repair assays

The well-established DR-GFP, EJ5-GFP, and SSA-GFP reporter assays[19,20] were used to evaluate the impact of DDX3X loss on homologous recombination, non-homologous end joining repair, and single-strand annealing repair, respectively, of induced double strand breaks. U2OS cells, containing an integrated copy of each reporter, were transfected with either scrambled control or DDX3X siRNA and seeded in 24-well plates using FuGENE® HD Transfection Reagent (Promega, Madison, WI, USA) as per manufacturer's instructions. Twenty-four hours later, media was refreshed and cells were transfected with the ISceI-pCAGGS vector or empty vector. Media was again refreshed after 12 hours and cells were allowed to grow for three more days. Samples were harvested and evaluated for percentage of GFP-positive cells using BD FACSCanto flow cytometer (BD Biosciences, Bedford, MA, USA). The experiment was conducted with triplicate independent transfections and analyzed using GraphPad Prism 9.3.1 (RRID:SCR_002798, San Diego, CA, USA).

Western blotting

Total cellular protein was extracted from cells and tumor tissue using the RIPA Lysis Buffer System (Santa Cruz Biotechnology, Dallas, TX, USA) as per manufacturer's instructions. Protein concentration was determined utilizing the RC DC™ Protein Assay (Bio-Rad Laboratories, Hercules, California, USA) as per the manufacturer's instructions. Serial dilutions of bovine serum albumin (BSA, Invitrogen-Thermo Fisher Scientific) were used to generate standard curves for protein quantification of experimental lysates. Samples were run on NuPAGE™ 4–12% Bis-Tris Protein gels (Invitrogen-Thermo Fisher Scientific) and transferred onto methanol-activated Immun-Blot® PVDF (polyvinylidene difluoride) Membranes (Bio-Rad Laboratories), followed by 1 hour blocking in 2% BSA in Tris-Buffered Saline, 0.1% Tween 20 Detergent (TBST, Sigma-Aldrich, St. Louis, MO, USA). Membranes were incubated with primary antibodies (Table S1) in 2% BSA TBST blocking solution overnight at 4°C and subsequently incubated with HRP-conjugated secondary antibodies (Table S1) diluted 1:10,000 in 4% BSA TBST for 1 hour at room temperature. Blots were developed using Clarity™ Western ECL Substrate (Bio-Rad Laboratories) and imaged using ChemiDoc™ Touch Imaging System (RRID:SCR_021693, Bio-Rad Laboratories). Antibodies were then stripped from blots using Restore Western Blot Stripping Buffer (Thermo Scientific) prior to incubation with additional primary antibodies. Adobe Photoshop 2021 (RRID:SCR_014199, Adobe) was used to globally process images for contrast, size, and brightness. Densitometry analysis was performed using ImageJ2 software (RRID:SCR_003070, NIH).

Immunoprecipitations

To perform immunoprecipitation of whole cell lysates for DDX3, mouse anti-DDX3 IgG_{2b} (C-4, RRID:AB_10844621, Santa Cruz Biotechnology) or rabbit anti-DDX3 IgG (RRID:AB _2910140, Abcam, Waltham, MA, USA) were conjugated to SureBeads™ Protein G (1614023) or Protein A (1614013) Magnetic Beads (Bio-Rad Laboratories), respectively. Conjugation was performed per manufacturer's instructions. Following conjugation of anti-DDX3 antibodies to the magnetic beads, whole cell lysates containing 500 μg of protein were applied to the beads and immunoprecipitation was performed using the manufacturer's instructions at 4°C. Western blotting was performed in parallel where rabbit primary antibodies (Table S1) were applied to blots containing samples from the mouse anti-DDX3 IgG_{2b} (C-4, RRID:AB_10844621, Santa Cruz

Biotechnology) pulldown and mouse primary antibodies (Table S1) were applied to blots containing the rabbit anti-DDX3 IgG (RRID:AB_2910140, Abcam, Waltham, MA, USA) pulldown samples.

Subcellular fractionations

Isolation and collection of cytoplasmic and nuclear cellular fractions of EWS cell lines was performed using NE PER Nuclear and Cytoplasmic Extraction Kit (PI78833, Thermo Scientific). Subcellular isolation of cytoplasmic and nuclear fractions was performed per manufacturer's instructions. In parallel, whole cell lysates were generated, as described above, per experiment. Western blots were then performed, as described above, for experimental analysis of each fraction.

Lentiviral Isolation and Transduction of RNaseH1 WT and RNaseH1 D210N

Lentiviral vectors ubc-Hu-RNASEH1-3xHA (RNaseH1 WT) and ubc-Hu-RNASEH1-D210N-Halo-3xHA (RNaseH1 D210N) were gifts from Dr. Teresa Bowman. Lentiviral particles were generated by transfecting HEK293T with RNaseH1 WT or RNaseH1 D210N using FuGENE® HD Transfection Reagent (Promega) per manufacturer's instructions. Viral supernatants were collected from transfected cultures and incubated in a 1:10 solution of 50% PEG 8000 and 1.5 M NaCl overnight at 4°C. Viral particles were then isolated via centrifugation, resuspended in serum-free RPMI 1640 media, and either used immediately or stored at −80°C. EWS cell lines were transduced with either $RNaseH1^{WT}$ or $RNaseH1^{D210N}$ lentiviral particles for 48 h at 37°C in 5% CO_2 prior to performing radiosensitization assays, described above.

QUANTIFICATION AND STATISTICAL ANALYSIS

Data were analyzed for statistical significance using GraphPad Prism software: Version 9.3.1(RRID:SCR_002798, GraphPad Software, San Diego, CA). A confidence level 0.05 or less was considered statistically significant for all analyses. Kaplan-Meier curves were analyzed for significance using the log rank (Mantel-Cox) test using R2 Genomics Platform (https://r2.amc.nl). Unpaired Student's *t* test was used when comparing two independent datasets. To compare the results of multiple datasets across one variable, data were analyzed using one-way analysis of variance with either Dunnett's or Šídák's multiple comparisons posttests. Two-way analysis of variance with Šídák's multiple comparisons posttest was applied to datasets with multiple comparisons across two variables. Two-way mixed effects analysis of variance with Tukey's multiple comparisons posttest was utilized to analyze the *in vivo* PDX growth data.